FRACTURE BEHAVIOR AND PROPERTIES OF FIBER-REINFORCED CEMENTED PASTE BACKFILL UNDER DIFFERENT DISPLACEMENT RATES

by

Senay Hagos

A thesis
submitted to the Faculty of Graduate Studies
in partial fulfillment of the requirements for the
Degree of Master of Science
in
Civil Engineering.

Supervisor

Dr. Liang Cui

Associate Professor – Dept. of Civil Engineering

Lakehead University
Thunder Bay, Ontario
August, 2024.

Abstract

Cemented paste backfills (CPB, comprising waste tailings, hydraulic binder, and water) are essential for safe and efficient underground mining production. Once delivered into underground excavations, CPB undergoes complex field conditions. Maintaining the engineering performance and mechanical stability of mine backfill mass, including fibers, can significantly enhance its mechanical behaviors (especially post-peak resistance) and CPB properties. Nevertheless, the field loading conditions are commonly featured in various loading rates. Therefore, to ensure backfill mass stability, it is essential to fully understand the effect of displacement rates on the mechanical behaviors and properties of fiber-reinforced-CPB (FR-CPB). This study examined the effect of different displacement rates (0.2mm/min, 1mm/min, 5mm/min, and 10mm/min) on the fracture behavior and properties of FR-CPB, which were prepared with three polypropylene fiber lengths (6mm, 13mm, and 19mm), and four fiber content (0.25%, 0.5%, 1%, and 1.5%) at three different curing times (7 days, 28 days, and 90 days). A comprehensive testing program was designed and performed, including semi-circular bend tests, end-notched disc bend tests, and SEM observations. The results demonstrate that load-displacement curves are sensitive to the changes in the displacement rate, with a higher displacement rate resulting in a higher peak load and post-peak resistance load. Moreover, it was also found that, compared with the influence of fiber content, the fiber length variation can interfere with the displacement-rate dependency of fracture properties to a greater extent. Furthermore, it is interesting to observe that excessive usage of fibers can cause material stiffness, fracture toughness, and fracture energy degradation. Moreover, a critical

loading rate (1mm/min) has been identified, which can cause significant changes in the rate of change in fracture properties. In terms of optimum usage of fibers, the results show that a fiber length of 13mm and a fiber content of 0.5% can maximize the fiber reinforcement effect on the improvement of fracture properties of CPB under different displacement rates. Therefore, the findings from this study can potentially promote the successful implementation of fiber reinforcement techniques in the mine backfill operation.

Acknowledgment

First and foremost, I thank my supervisor, Dr. Liang Cui, P.Eng. His dedication and mentorship helped me to finish my thesis successfully. I am grateful to my family and friends for their countless support. I would also like to thank lab technician Cory for showing me the lab instruments and my thesis examiners, Dr. Baoqiang Liao and Dr. Jian Deng.

Finally, my greatest appreciation goes to my father, Ghebremichael Hagos, for his encouragement and assistance in getting my M.Sc.

Contents

List of Figures

List of Tables

Chapter One Introduction

1.1 Background

Mineral resources are the foundation of the long-term growth of the human economy and society. Yet, their extraction unavoidably jeopardizes the ecological environment, especially the solid wastes (e.g., waste rock, tailings) produced by mining activity and mineral processing. Most of these tailings were piled up in tailings storage facilities (TSF, such as embankments, dams, and dykes), the construction of which occupies a large area of land. The tailings deposits are likely to cause tailings dam collapse, environmental pollution, and other harmful impacts. [Wang et al., 2017]. There are three methods to backfill stopes: Hydraulic fill involves mixing tailings with water to create a slurry, which is then pumped into the voids left by mining operations, then the water is later drained, leaving the solid material to fill the space; Cemented paste fill (CPF) involves the tailings are mixed with a binder (cement and water) to form a thick paste, then pumped into the voids, the cement helps to solidify the fill, providing additional support; and Uncemented paste fill is similar to CPF without the additional cement, relies on the natural settling and consolidation of the material to fill the voids.

Cemented paste backfill (CPB) is a specialized mining and civil engineering technique to manage and safely dispose of mine tailings or waste materials [Belem et al., 2002]. It involves mixing the tailings with cement and water to create a paste-like material that can be used to backfill underground mine workings or fill voids in the ground. The advantages of CPB are numerous; some of them can be reclaiming water, processing reagents, and energy; maximizing the density of mine tailings, thus minimizing the footprints of surface tailings ponds;

minimizing the risk of tailings ponds failure; increasing mining safety, efficiency, and productivity due to increased stability of underground voids [Deb et al., 2017, Edraki et al., 2014]. To avoid the geological disasters caused by tailing failure, CPB was proposed and first implemented at the Bad Grund Mine, Germany, in 1979 [Hustrulid et., 2001]. The environmental pollution by tailings is reduced, and the method supports underground voids (Figure 1.1). In general, CPB is a cement-based material with a particular strength formed by mixing cement, tailings, and water, and it is commonly evaluated by its unconfined compressive strength (UCS), which ranges from 0.2–4 MPa [Koohestani et al., 2016]. However, to overcome sudden failure, a better approach is to add fibers to the mix under complex in-situ loading [Sun et al., 2018].

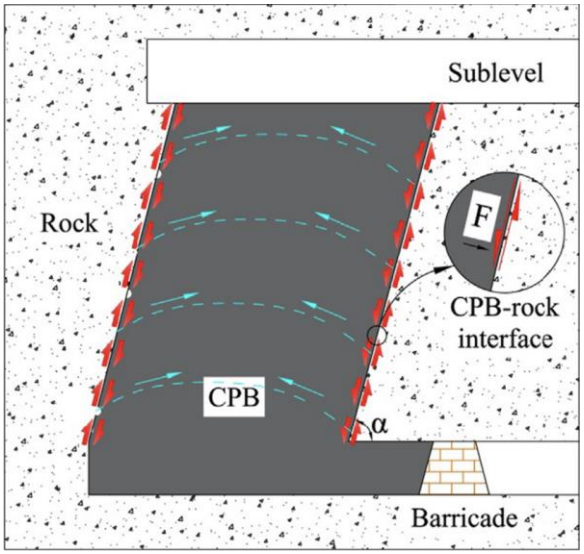

Figure 1.1: Underground CPB structure and surrounding rock [Kun et al., 2018].

Scenarios of fracture modes in mining stopes can be explained as: mode-I occurs in the roof contact between CPB and rock; mode-II occurs when the secondary stope is mined out when CPB fills the primary stope, and then biaxial stress comes along when one side is left without

support, resulting in shear stress arising inside the CPB; and mode-III occurs at CPB-rock interface (Figure 1.1) as it is affected by shear and tensile stresses.

1.2 Problem Statement

The CPB structure is subjected to complex loading conditions after placement into underground voids (called stopes). Specifically, due to the biaxial loading conditions, tensile stress dominates the mechanical response of CPB near the exposed surfaces. Meanwhile, the polyaxial loading results in the formation of tensile and shear stresses inside the CPB mass. As the tensile and shear stresses develop and concentrate, the cracks may initiate and propagate in the CPB's cemented-based matrix, thereby governing its macroscale failure process. Correspondingly, the resistance to the cracks induced by tensile and shear stress plays a central role in assessing the mechanical performance of CPB materials. Most importantly, as natural mineral resources are continuously extracted, the underground mining depth has reached more than 1000 meters [Pereira et al., 2010; Marcos et al., 2024; Blikharskyy et al., 2019]. The deep mine stopes are features with extremely high geo-stress and considerable stope contraction, which cause complex external loading conditions on mine backfill materials. As a result, the peak strength-based design may impose a risk on the mechanical stability of backfill structures due to the weak strength of CPB relative to the geo-stress level in the surrounding rock. Correspondingly, the residual resistance (i.e., the post-peak resistance) of CPB materials plays a crucial role in the stability of backfill structure in deep mines. However, conventional methods to improve the mechanical behavior and properties of CPB rely highly on using hydraulic binders in terms of their types and content [Ghirian et al., 2017; Liang et al., 2023]. However, it is important to point

out that the hydraulic binder is effective for changes in peak strength rather than post-peak resistance. It has been widely observed that a higher peak strength as the adjustment of the binder is consistently accompanied by a sharper drop after the peak value, which indicates an enhanced brittle response. Therefore, the adjustment of the hydraulic binder cannot simultaneously improve both the peak and post-peak resistance of CPB materials. Considering the complex loading conditions in deep mines, post-peak resistance, and response must be fully considered in the engineering design of backfill materials. In this regard, the fiber reinforcement technique has been considered a promising approach to improve the residual response of CPB [Consoli et al., 2012].

Moreover, it has been widely observed that cement-based materials show loading-rate-dependent mechanical properties and behavior. For instance, as the loading rate increases, material peak strength, fracture energy, and crack propagation pattern can dramatically deviate from the counterparts measured under static loading conditions. Due to the mining activities (e.g., blast operation, machinery vibration induced by crawler-type loading machine) and underground geo-stress changes (e.g., contraction of stopes and seismic events), mine backfill materials commonly suffer different loading rates in underground mines [Zhang et al., 2009; Zhang et al., 2010; Lu et al., 2020]. Correspondingly, it is essential to investigate the dependence of fracture behavior and properties of fiber-reinforced CPB (FR-CPB) to facilitate the successful implementation of fiber reinforcement techniques in CPB materials. However, no studies have been designed to systematically study the sensitivity of fracture behavior and properties of FR-CPB to the loading rates. Therefore, to narrow the research gap, the objectives

of this study are to experimentally investigate the influence of loading rates on (1) fracture behavior (i.e., the load-displacement curves) under mode-I (pure tensile), mode-II (pure in-plane shear), and mode-III (pure out-of-plane shear) loading conditions and (2) fracture properties, including material stiffness, fracture toughness, and fracture energy of FR-CPB. Moreover, to offer in-depth insight into the effectiveness of the fiber reinforcement technique, various fiber lengths and fiber content will be employed to student their influence on the loading-rate dependent behavior and properties of CPB from early (7 days) to advanced (90 days) curing times.

1.3 Research Methodology

The present experimental study consists of several mechanical tests and microstructure observations to reveal the loading-rate-dependent fracture behavior and properties of FR-CPB under different loading conditions at various curing times.

First, the mix recipe of FR-CPB consists of a constant cement content (Cc) of 4.5% and a water-to-tailing ratio (WTR) of 0.36. The WTR is the value of the mass of water divided by the mass of tailing. This study took three fiber lengths of polypropylene (PP) fiber: 6mm, 13mm, and 19mm. For each length of PP, five different fiber contents are in the mix recipe (0%, 0.25%, 0.5%, 1%, and 1.5%). The obtained FR-CPB samples are cured in the laboratory environment for three different curing times (7, 28, and 90 days).

Second, the target FR-CPB samples will be studied by two different mechanical tests, including semi-circular bend (SCB) tests and end-notch disk bend (ENDB) tests, under four different

displacement rates (0.2, 1, 5, and 10 mm/min). SCB tests are used to investigate the fracture behavior of mode-I and mode-II loading conditions. ENDB tests are used to examine the loading-rate-dependent fracture behavior of CPB under mode-III loading conditions. The measured load-displacement curves from SCB and ENDB tests are utilized to analyze the fracture behavior of FR-CPB under various loading rates. Meanwhile, the fracture properties, including materials stiffness, fracture toughness, and fracture energy, can be extracted from the measured load-displacement curves. Then, based on the measured data, the dependency of fracture properties on loading rate can be identified.

In addition, auxiliary scanning electron electroscope (SEM) tests are conducted to reveal the microstructure changes between fiber, tailing, cement, and water content at different curing times (7, 28, and 90 days). The microstructure can facilitate the identification of governing mechanisms responsible for the evolution of fracture properties of FR-CPB at different curing times.

1.4 Thesis Organization

This research thesis is arranged into five chapters. Chapter One is the introduction to the research. Chapter two explains the literature studies related to CPB and FR-CPB. Chapter three shows the experimental testing program, which includes the preparation of FR-CPB samples, mechanical testing methods, and measurement and calculation of experimental data. Chapter four describes the experimental results and discussion on the effect of loading rate on the fracture behavior (i.e., load-displacement curves) and fracture properties (i.e., material

stiffness, fracture toughness, and fracture energy) of FR-CPB with various fiber content and fiber lengths at different curing times. Finally, chapter five presents the conclusions and recommendations for future work.

Chapter Two Literature Review

2.1 Background

Cemented paste backfills (CPB), which mainly consist of thickened tailings (with a solid percentage of 70–85%), binder (typically 3–7 wt%), and water, are prepared in a backfill plant usually located on the mine surface [Yilmaz et al., 2016]. The binder is mainly prepared with ordinary Portland cement; its composition is explained in Table 2.2. The mechanical failure of CPB structures not only jeopardizes mining productivity but also dramatically threatens the safety of underground workers and has substantial financial ramifications for the mine [Hassani and Archibald, 1998]. During actual filling operations, deposit mining stress disturbances, blast stress waves, flying rocks, poor geological formations, and poor filling effects, as well as time and temperature-dependent shrinkage of the filling body and expansion of the filling body due to sulfate erosion from inside or outside, are very prone to generate a large number of initial defects such as joints and fissures inside the filling body [Fang et al., 2020]. This means that the arching effect can reduce the amount of cement consumed by up to 75% of the cost of CPB [Kun et al., 2021; Kun et al., 2019]. It is the most common of the backfill composite types due to the following advantages: reduced cement consumption, low operation costs, increased mining cycle, and high ore recovery [Cao et al., 2018; Xu, 2018]. CPB forms a structural support stope with specific strength through hydration to control surface subsidence, reduce dilution loss rate, and improve recovery rate.

The quartz (silica) tailings were selected to prepare backfill materials composed of 99.8% SiO_2 (Table 2.1), identified as the primary mineral in hard rock mines in Canada. The particle size distribution is shown in Figure 2.1 [Libos, 2021]. The matrix provides only marginal reinforcement to the encasing rock strata. Given the prevalence of fractures in deep environments, it is imperative to enhance the interactions and consequences when CPB is subjected. A continuous investigation is essential to ensure the structural integrity and longevity of CPB in complex geological settings. After fracture, CPB loses resistance and can no longer sustain any loads. This can be modified using fiber in the matrix [Jiaxu et al., 2022; Consoli et al., 2017; Cao et al., 2019]. The fibers have the potential to improve the post-peak resistance of the CPB. Numerous studies [Iarley et al., 2020; Li et al., 2016; Liang et al., 2023] have been done on FR-CPB to understand mechanical behavior. This research emphasizes changing the displacement rates to show the mechanical and material properties of FR-CPB.

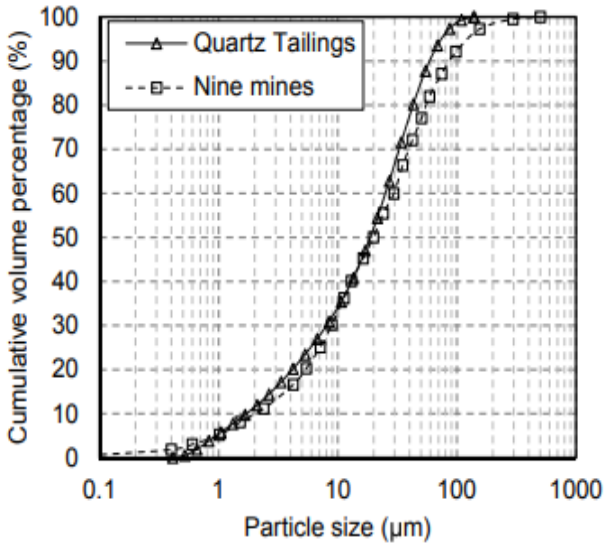

Figure 2.1: Comparison of particle size distribution between the adapted quartz and natural tailings [Libos, 2021].

Table 2.1 Composition of Tailings [Cao et al., 2019].

Parameters	SiO_2	Al_2O_3	Cao	MgO	P	Fe	S	Au
Varieties (%)	65.7	14.3	1.88	0.49	0.08	3.05	0.13	<0.01

Table 2.2 Physical and chemical properties of ordinary Portland cement [Cao et al., 2019].

Parameters	SiO_2	Fe_2O_3	Al_2O_3	MgO	CaO	SO_3	Specific surface area
Varieties (%)	21.36	3.21	4.92	3.41	62.33	1.92	0.13

2.2 Effect of Fiber Reinforcement on the Mechanical Behavior and Properties of CPB

Fibers can postpone or restrain cracks' propagation by forming close interactions between fibers and matrix, thus improving the bearing capacity of soil structure [Yetimoglu et al., 2003; Tang et al., 2007]. Moreover, Yi et al. [2015] found that fiber usage contributes more to UCS improvement than cement hydration and reduces the post-strength loss of CPB. The engineering performance of fiber reinforcement depends on the interaction between fiber and matrix [Nezhad et al., 2021]. Xu et al. [2020] revealed that the inclusion of fibers affects the volume change of CPB under shear stress. [Xue et al., 2019] examined the influence of fiber types (such as polypropylene, polyacrylonitrile, and glass fibers) on the compressive strength of CPB and found that the reinforcing effect of polypropylene fiber is much better than the other two fibers. The fact that the cost of cement accounts for 20% to 40% of the mining activities, replacing specific cement with fibers can considerably decrease the cost of CPB [Wang et al., 2021].

Polypropylene fiber is a synthetic material widely applied in civil engineering and material science due to its cost-effectiveness, ease of manufacturing, and acid and alkali resistance [Yu et al., 2001; Ranjbar et al., 2016]. Pakravan et al. [2017] found that low-strength soft fibers were better than rigid fibers with high strength and moduli in improving ductility and reducing cracking behavior. Although PP fiber reduces the compressive strength of concrete, the reduction is not significant because of the high toughness and durability of such fiber [Farina et al., 2018; Kim et al., 2018]. Yi et al. [2015] conducted a series of uniaxial compressive strength (UCS) experiments on the cemented backfills prepared using polypropylene fibers and sand tailings from Western Australia's nickel ore. The obtained test results indicated that fiber addition to the backfill significantly reduced the post-peak strength loss and increased the potential of the mine fill integrity and self-bearing capacity. Ma et al. [2016] adopted polypropylene fiber-reinforced paste backfill samples to improve their brittleness rate. They showed that adding fiber to the fill slightly increases the peak compressive strength and prevents crack propagation and elongation within the cemented backfill. Besides, Consoli et al. [2017] experimentally studied the durability and strength properties of fiber-reinforced, high-density gold tailings-silicate cement composites. These authors found that fiber inclusions decrease samples' mass loss after wetting/drying cycles and increase the corresponding compressive strengths linked with the adjusted porosity/cement index.

The addition of fibers can improve the flexural strength and toughness of cement composite, and the bending deformation of the backfill samples depends on the mixing intensity characteristics at the macro and micro levels, inclusive of cement properties, water-cement

ratio, and fiber type and content [Deng et al., 2016]. Experimental studies have been conducted to probe the fiber reinforcement technique's effectiveness in improving conventional geomechanical behaviors and properties of CPB materials [Li J et al., 2022]. Fang and Cui [2023] found that the development of matric suction can contribute to the shear strength of unsaturated FR-CPB. For the pre-peak branch, FR-CPB demonstrates a linear load-displacement behavior despite the ages of the specimens. This confirms the validity of linear elastic fracture mechanics for FR-CPB materials. Moreover, when the warmer curing temperature is applied, the linear pre-peak branch is further enhanced and shows a higher material stiffness.

Al-Mashhadani et al. [2018] found that adding fibers improved the mechanical strength properties of geopolymer composites, and the existence of steel/polyvinyl-alcohol fiber increased the corresponding flexural strength. Similar results from hybrid steel and polypropylene fiber-reinforced geopolymer were also reported [Sukontasukkul et al., 2018]. In addition, an increase in the fiber content from 0.5% to 1.5% increased the flexural strength from 3% to 124% for fiber with a smaller aspect ratio of 65 [W. Abbass et al., 2018]. The strength gain of FR-CPB samples showed an increasing trend as fiber content increased, with polypropylene fiber being better than polyacrylonitrile and glass fiber [Cao et al., 2019].

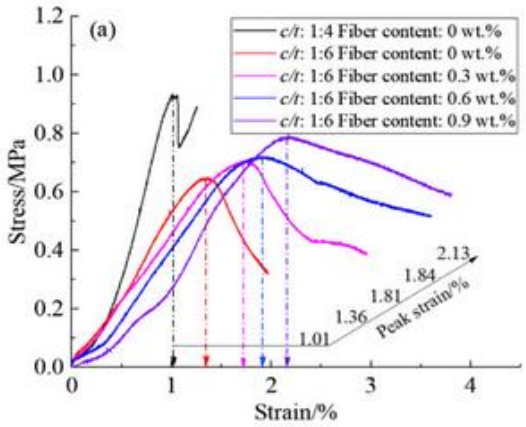

Figure 2.2 Effect of PP on stress-strain curve 3-days cured [Cao et al., 2019].

2.3 Effect of Loading Rates on the Mechanical Behavior of CPB

Displacement rates refer to the speed at which a load is applied to a material, while strain refers to the deformation or change in shape that a material undergoes in response to the load. The loading rate (LR) dependency of rock is one of the fundamental mechanical properties essential in understanding the mechanism of earthquake and geological tectonic movements and estimating the long-term stability of underground structures, e.g., mining roadways and underground storage [Wasantha, 2015]. One solution to these challenges is using cemented paste backfill as secondary pillars to ensure the stability of the underground excavations [Tang et al., 2021]. Okubo et al. [1990] observed that the triaxial compressive strength (TCS) increased proportionally concerning the logarithm of the loading rate and that the loading rate dependence of TCS was similar to that of UCS. At lower loading rates, cracks have sufficient time to propagate and connect, which can decrease peak strength. Experimental studies have shown that CPB exhibits rate-dependent behavior under compressive loading. CPB exhibits a higher strength and stiffness at low loading rates than at high loading rates. The binder has

more time to develop strength and form a strong bond between the tailings particles at low displacement rates.

Mechanical behavior refers to how materials respond to external forces or loads. This can include many physical properties, such as strength, stiffness, flexibility, toughness, hardness, and elasticity. The mechanical behavior of CPB is an essential consideration in the design and operation of the backfill system. The mechanical properties of backfill are affected by factors such as LR and PF (prefabricated fractures). A lower LR leads to the development of micro-defects inside the filling body, which expand into micro-cracks during elastic deformation, reducing the energy storage capacity. On the other hand, a higher LR inhibits the development of defects, strengthening the resistance to deformation and increasing energy storage capacity, leading to an improvement in UCS and EM. The critical LR for low-strength filling bodies under quasi-static loading is determined by the properties of the filling body itself and external factors. The presence of PF is equivalent to the arrangement of initial defects, which results in stress concentrations and the early development of cracks in the PF area. The LRs were selected as 0.1, 0.25, 0.5, 1, and 2 mm/min (the selected LR was the typical LR for the UCS test of the filling body). The samples were placed on the loading end of the press. The displacement loading mode was selected. The stress and strain data were automatically recorded during the loading process [Song et al., 2022]. UCS and EM of PF-CPB and CPB under different LRs are shown in Figure 2.3. UCS was positively correlated with LR. As LR increased (Figure 2.3.a), UCS increased as a polynomial function with the increasing rate decreasing ($R2 > 0.890$). EM of the filling body raised with the increase in LR regardless of the presence of PF (Figure 2.3.b).

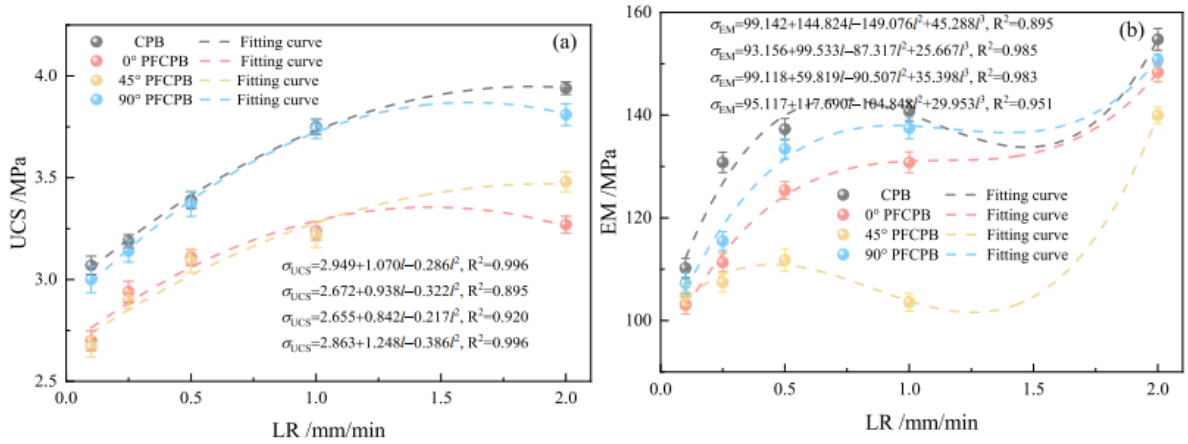

Figure 2.3. UCS and EM (elastic modulus) of the filling body (a: UCS; b: EM) [Song et al., 2022].

The mechanical characteristics of backfill were evaluated at the mid-term curing time (i.e., up to 91 days) through uniaxial compression tests and triaxial compression tests. The hydration rate depends on the binder percentage. When backfilling can only be done in a single sequence (for various mine operations reasons), the binder should be able to generate a strength of about 700 kPa in the short (28 days) and a strength of about 1000 kPa at the term (more than 91 days) in paste backfill [Tikou et al., 2000]. Li et al. [2021] reported that the UCS of CPB increased significantly as the loading rate increased from 2 mm/min to 8 mm/min. The maximum displacement required to reach the peak stress gradually decreases when the loading rate increases [Zhan et al., 2021]. The change in fiber length, displacement rates, and fiber content's effect on FR-CPB fracture behavior are discussed in this research work.

2.4 Effect of Loading Rates on the Mechanical Properties of CPB

Mechanical properties of mine backfill materials are significantly influenced by the loading rates, as evidenced by various studies. Wang et al. [2023] reported that as the loading rate increases, the compressive strength of the backfill body linearly increases, peak strain rises in an S-shaped manner, and the modulus of elasticity initially increases and then decreases. Tensile failure is the dominant mode, with multiple failures occurring at higher loading rates, impacting crack distribution. Song et al. [2022] conducted a study on prefabricated fracture CPB and examined the mechanical behavior and cracking mechanism under varying loading rates. The research delves into how different loading rates impact the energy evolution and, consequently, the mechanical properties of the CPB. By analyzing the energy evolution, the study sheds light on how loading rates influence the overall mechanical behavior and cracking mechanism of the backfill material. Xiu et al. [2021] investigated the impact of loading rate on the UCS of CPB. It has been found that, as shown in Figure 2.4, an increase in loading rate led to an increase in CPB's UCS. It was also observed that the loading rate effect on the UCS behavior of CPB was more significant at higher stress levels. Chen et al. [2021] utilized a Split Hopkinson pressure bar (SHPB) and revealed that a higher strain rate resulted in larger increases in dynamic compressive strength compared to static loading. Additionally, the dynamic compressive strength of CPB showed an exponential correlation with the strain rate. Increasing cement content, tailings content, and curing age improved dynamic compressive strength and elastic modulus. Under dynamic loading, CPB experienced more severe damage with enhanced local

damage and the formation of fine cracks due to the inability to dissipate high strain rate stress wave energy efficiently.

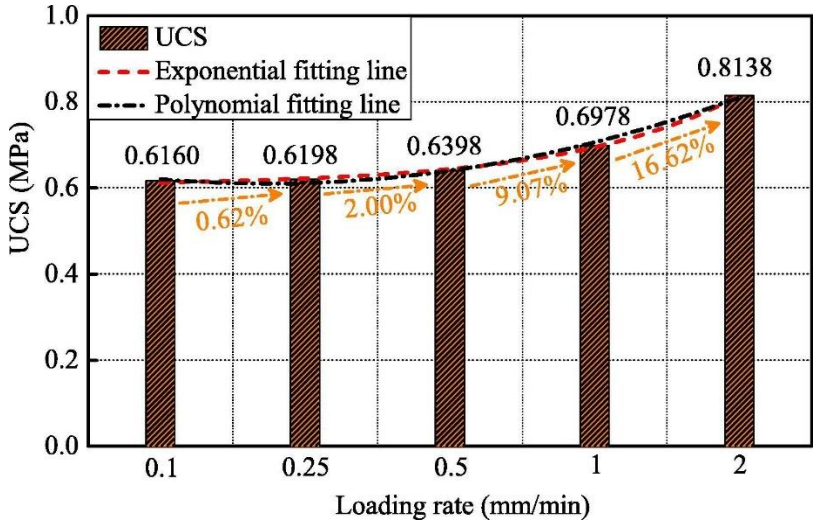

Figure 2.4. Effect of loading rate on the UCS of CPB [Xiu et al., 2021].

Although extensive studies have been conducted to investigate loading-rate-dependent behavior and properties of CPB, very limited studies have been devoted to the analysis of mechanical properties of FR-CPB under different loading rates. For example, Xue et al. [2021] experimentally investigated the reinforcement effect of polypropylene fiber on the dynamic properties of CPB under SHPB impact loading. It has been found that the addition of polypropylene fiber to CPB resulted in an increase in the dynamic properties of the backfill material under SHPB impact loading. The reinforcement effect of polypropylene fiber was observed to enhance the energy absorption capacity and dynamic strength of the CPB, making it more suitable for applications requiring resistance to dynamic loading. Except for the above-mentioned study, no further work has been conducted regarding loading-rate-dependent

mechanical behavior and properties of FR-CPB, which prevents the successful implementation of fiber reinforcement into the mine backfill materials design.

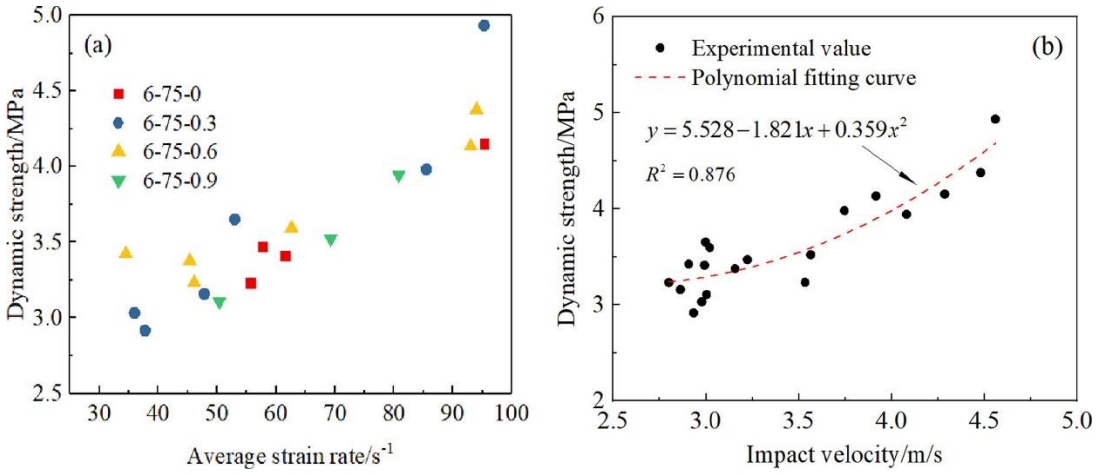

Figure 2.5. Effect of strain rate on the dynamic strength of FR-CPB [Xue et al., 2021].

2.5 Summary

Previous studies have confirmed that the usage of discrete fibers can only improve the mechanical behavior, especially post-peak response, of CPB materials. Post-peak behavior is crucial for the in-situ performance of CPB structures used in deep mines. This is because the corresponding geo-stress is greater than the peak strength of backfill materials. Correspondingly, the improvement of the post-peak behavior of CPB can effectively improve the mechanical stability of CPB in deep mines.

However, previous studies focused mainly on the mechanical response of CPB materials under UCS tests, which is due to the wide usage of strength-based design methods. Correspondingly, the elastoplastic theory serves as the basis for the engineering design of CPB materials.

However, as cement-based materials, the damage accumulation and failure process are governed by the crack growth in the CPB matrix rather than the accumulation of permanent strain. Consequently, the crack behavior and associated fracture properties must be fully considered and evaluated for the engineering application of CPB technology.

To evaluate the fracture behavior and properties of FR-CPB, it is of practical importance to consider the in-situ loading conditions. Due to the combined effect of mining activities (e.g., blasting operation and usage of various mine loading machines) and changes in geo-stresses (e.g., contraction of rock stopes and seismic events), mine backfill materials encounter complex loadings with various loading rates. Therefore, the investigation of loading-rate-dependent fracture behavior and properties of FR-CPB can offer valuable information to the engineering design and application of mine backfill technology in practice. However, no studies have been designed to address this research gap, which motivates the present study. Correspondingly, this study aims to systematically investigate the effects of loading rates on the fracture behavior and properties of FR-CPB with different fiber lengths and content at different curing times. The obtained results will potentially improve the effective usage of fiber reinforcement techniques and promote the safe design of CPB materials in practice.

Chapter Three Experimental Testing Program

3.1 Materials

The primary material used for this study is artificial tailings, which consist of 98% pure silica powder. Artificial tailings were chosen due to their ease of access and the consistency of the material [Qi et al., 2019; Hu et al., 2023]. As the tailings from a field are non-homogeneous material, they can cause variance in the results. Ordinary Portland cement (OPC) is used to bind the artificial tailings. The fiber used in this research is polypropylene fiber $(C_3H_6)_n$, a synthetic fiber made by propylene polymerization (Figure 3.1). It is lightweight and has 398 MPa tensile strength, a density of 0.91 g/cm^3, Young's modulus of 3.85 GPa, and corrosion resistance. Three different fiber lengths (Fl), 6mm, 13mm, and 19 mm, and five fiber contents (Fc) of 0%, 0.25%, 0.5%, 1%, and 1.5% were used to prepare FR-CPB samples. The tap water in the lab is used to mix the ingredients.

Figure 3.1. Polypropylene fiber (PP) with 13mm length.

3.2 Mix recipe and curing method

The mix recipe will be varied for each test to determine the effects of length and percentage content of PP fiber. The mix recipe was prepared using the specified Cement content (Cc=4.5%) and water tailing ratio (WTR=0.36) for all samples. Based on the volume of the curing cylinder and an assumed density of CPB of 20 kN/m^3, the mass of the sample could be determined. Then, the mass of cement, PP fiber, water, and tailings can be calculated using several equations. Two equations are used to substitute the other variables for the cement mass. Equation 3.3 can then be used to determine the tailing mass of CPB. Finally, using the water-to-tailings ratio, the mass of water was determined. A summary of the mix design for each formation is provided in Table 3.1. The detailed determination of the mass of each mixing component is summarized via the following calculation procedures.

The cylindrical molds have dimensions of 20 cm in height and 10 cm in diameter. Therefore, the volume of the mold is calculated as:

$$V = A*H = \pi r^2 H = \pi*5^2*20 = 1570.8 \text{ cm}^3 = 0.0015708 \text{ m}^3 \quad (3.1)$$

where A is the area of the base of the mold (circular). $A = \pi r^2$ [cm^2]; H is the height of the mold [cm]; and V is the total volume of the mold [cm^3].

Assuming a density of CPB, Y_{cpb} equal to 20 kN/m^3, the mass of CPB is

$$M=Y_{cpb}*V = \frac{20*1000}{9.81} * 0.0015708 \text{ m}^3 = 3.202446 \text{ kg}. \quad (3.2)$$

Based on the adopted mix recipe, cement mass = 1 kg, cement content (Cc) = 4.5%, WTR = 0.36, and fiber content (Fc)= 0%; 0.25%; 0.5%; 1%; 1.5%.

For instance, when the fiber content is 0% (control sample), the mass of tailing, water, fiber, and cement calculation is shown below:

$$\text{Tailing mass (kg)} = \left(1 - \frac{Cc}{100}\right) * \left(\frac{Cement\ mass}{Cc/100}\right) \quad (3.3)$$

Tailing mass (kg)=(1-0.0045) * (222.22)= 21.2222 kg.

$$\text{Water mass (kg)} = \text{WTR} * \text{Tailing mass} \quad (3.4)$$

Water mass (kg)= 0.36 * 21.22222 = 7.64 kg.

$$\text{Fiber (kg)} = (\text{Tailing mass} + \text{Water mass}) * \frac{Fiber\ content}{100} \quad (3.5)$$

Fiber (kg)=(21.2222 kg+ 7.64kg) * 0= 0 kg.

$$\text{Total mass of CPB} = \text{Cement mass} + \text{Water mass} + \text{Tailing mass} + \text{Fiber mass} \quad (3.6)$$

Total mass of CPB (kg) =1kg + 7.64kg + 21.2222kg + 0 kg= 29.86222 kg.

Calculated cement, water, fiber, and tailing mass values per mold are given below:

$$\text{Cement mass (kg)} = \frac{Cement\ mass}{Total\ mass\ of\ CPB} * mass\ of\ CPB\ per\ mold \quad (3.7)$$

Cement mass (kg) = $\frac{1\ kg}{29.86222kg} * 3.202446kg$ = 0.107277 kg.

$$\text{Water mass (kg)} = \frac{Water\ mass}{Total\ mass\ of\ CPB} * mass\ of\ CPB\ per\ mold \quad (3.8)$$

Water mass (kg) = $\frac{7.64\ kg}{29.86222kg} * 3.202446kg$ = 0.81959 kg.

$$\text{Tailing mass (kg)} = \frac{Tailing\ mass}{Total\ mass\ of\ CPB} * mass\ of\ CPB\ per\ mold \quad (3.9)$$

Tailing mass (kg) = $\frac{21.2222\ kg}{29.86222kg} * 3.202446kg$ = 2.2276658 kg.

$$\text{Fiber mass (kg)} = \frac{Fiber\ mass}{Total\ mass\ of\ CPB} * mass\ of\ CPB\ per\ mold \quad (3.10)$$

Fiber mass (kg) = $\frac{0\,kg}{29.86222kg} * 3.202446kg$ = 0 kg.

Table 3.1. Mix recipe for preparation of CPB samples.

Parameters	Control CPB	FR-CPB			
Fl(mm)	-	6,13,19	6,13,19	6,13,19	6,13,19
Fc(%)	0	0.25	0.50	1	1.50
Cc(g)	107.28	107.02	106.76	106.25	105.74
Tailing(g)	2276.66	2271.17	2265.71	2254.87	2244.12
Water(g)	819.6	817.62	815.66	811.75	807.88
Fiber(g)	0	7.72	15.41	30.67	45.78

*Fl: fiber length, Fc: fiber content, and Cc: cement content.

3.3 Mechanical Testing Methods

To study the fracture behavior and properties of FR-CPB under different loading rates (0.2, 1, 5, and 10mm/min), two mechanical testing methods, including semi-circular bend (SCB) tests and end-notched disc bend (ENDB) tests, were conducted. SCB tests were used to study the tensile (i.e., mode-I) and in-plane (i.e., mode-II) fracture behavior of FR-CPB via the adjustment of the inclination angle of notches into the disc samples. The ENDB tests were employed to study the out-of-plane (i.e., mode-III) fracture behavior of FR-CPB under different displacement rates.

For the testing sample preparation, an air hose pushes the molds out from the cylinder

after reaching their assigned curing time (7, 28, and 90 days). One cylinder is cut into three small cylinders with 5 cm thickness using a table saw. For mode-I and mode-II SCB tests, the cylindrical samples are cut again to semi-circular with a 10 cm diameter, making six samples of each cylindrical sample. A vertical notch of 25 cm (see Figure 3.2.a) is introduced to the semi-circular sample for mode-I SCB tests, while an inclined notch with an inclined angle of 40° is prepared for the mode-II SCB tests (Figure 3.2.b), respectively. For mode-III ENDB tests, the cylinder disk with 5 cm possesses a 2 cm central notch (Figure 3.2.c). It is undergone by making a 60° angle between the central notch and top loading bar.

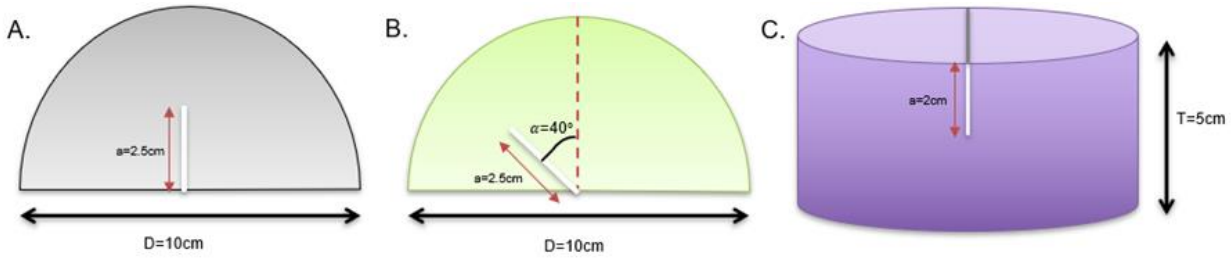

Figure 3.2. Specimen geometry and dimension: a) mode-I SCB specimen, (b) mode-II SCB specimen, (c) mode-III ENDB specimen.

The displacement rates used in this study are set to 0.2, 1, 5, and 10 mm/min. 1404 samples were tested using the SCB and ENDB testing methods for this research thesis. The crack propagation can be observed in Figure 3.3 for three modes of fractures. Data is calculated using a PC connected to a loading frame, displacement transducer, and datalogger system. For SCB, the load cell has a spacing of 8.13cm and 5cm for mode-I and mode-II, respectively. Also, for ENDB samples, the spacing is 9cm, as used in mode-III. Personal protective equipment (PPE) measures are used during all the procedures.

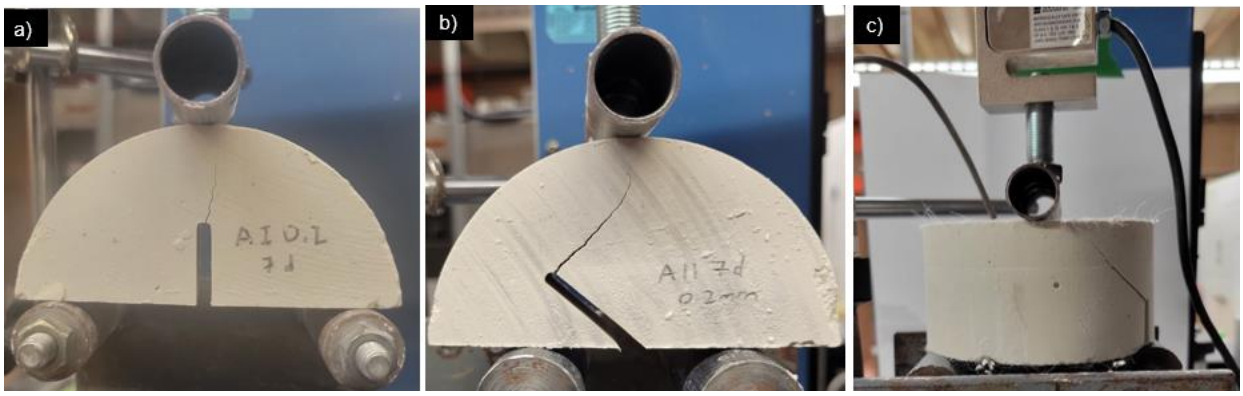

Figure 3.3. Experimental setup of fracture toughness measurement with crack propagation: (a) mode-I SCB test, (b) mode-II SCB test, and (c) mode-III ENDB test.

3.4 Auxiliary Analysis

The control CPB without fiber reinforcement and FR-CPB matrix microscopic image was produced as an auxiliary analysis using a scanning electron microscope (SEM). The SEM samples are collected from three curing times (7, 28, and 90 days) and placed in an oven at 50°C for 48 hours. Then, samples are put in a ziploc bag to keep the dry sample in the laboratory.

3.5 Determination methods of fracture properties

The fracture toughness can be found using the equations shown below:

Mode-I fracture toughness (based on the semi-circular specimen with a vertical notch):

$$Ki = \frac{P}{DT}\sqrt{\pi a}\, Yi \tag{3.11}$$

Where,

P is the maximum force (peak value of force vs. displacement curve) (N),

D is the diameter of the semi-circular specimen (m),

T is the thickness of the semi-circular specimen (m),

a is the notch length (m),

Yi is the normalized stress intensity factor for mode I (Yi=6.52) (dimensionless) [Ayatollahi et al., 2005]

Mode-II fracture toughness (based on the semicircular specimen with an inclined notch (α=40°)):

$$Kii = \frac{P}{DT}\sqrt{\pi a}\,Yii \tag{3.12}$$

Where,

P is the maximum force (peak value of force vs. displacement curve) (N),

D is the diameter of the semi-circular specimen (m),

T is the thickness of the semi-circular specimen (m),

a is the notch length (m),

Yii is the normalized stress intensity factor for mode-II (for your study, Yii=1.072) (dimensionless) [Ayatollahi et al., 2005]

Fracture toughness K has a unit of kPa·m$^{1/2}$. After you use the formulae mentioned above to calculate the K, you will obtain the K with a unit of kPa·m$^{1/2}$.

For these samples, D=0.1m, T=0.05m, and a=0.025m are constant throughout the mode-I and II tests. The equations will be simplified:

Ki= 365.445P [Pa$\sqrt{m}$]. (3.13)

Kii= 60.08P [Pa$\sqrt{m}$]. (3.14)

Mode-III samples are prepared by cutting a notch into a whole disk. The samples are loaded at four displacement rates (0.2, 1, 5, and 10 mm/min), and the load-displacement curve is logged. The fracture toughness, K_{III}, is calculated using the following equation:
Mode-III fracture toughness (based on ENDB tests with an inclined notch (β=60°)):

$$Kiii = \frac{P}{DB^2}\sqrt{\pi a}\, Yiii \tag{3.15}$$

Where,

a: the depth of notch (a=0.02m)

B: the thickness of the disc specimen (B=0.05m)

S: the horizontal distance between central and edge bars (S=0.045m)

R: radius of the disc specimen(0.05m)

β: inclination of notch line w.r.t. the central bar (β=60°.)

Yiii: is the normalized stress intensity factor for mode-III (Yiii= 0.0713) [Aliha et al., 2015]

The simplified equation when the constants are calculated is:

Kiii= 38.6P [Pa$\sqrt{m}$]. (3.16)

The stiffness (N/mm) of the sample is found from the load-displacement curve by calculating the slope in pre-peak. Two data points, including 40% and 60% of peak load along the pre-peak branch, are chosen to evaluate the material stiffness (i.e., the slope of the straight line portion between 40% and 60% of peak load).

$$k_m = \frac{60\%F_p - 40\%F_p}{D_{60} - D_{40}} \tag{3.17}$$

where F_P is the peak force (N), D_{60} is the displacement corresponding to 60% F_P, and D_{40} is the displacement corresponding to 40% F_P.

The crack initiation (Ec) and fracture energy (Ef) energy were calculated for all samples. Those fracture properties are computed from load Vs displacement curves. Ec (mJ) and Ef (mJ) are defined by the enclosed area beneath the curve until peak load and load value reach zero, respectively. Fracture properties are essential in understanding CPB's mechanical properties and behaviors when designing backfill. Fracture toughness and stiffness are essential designs based on the stress method. On the other hand, fracture energy is applied when designed through the energy method.

Chapter Four Experimental Results

4.1 Effect of displacement rates on load-displacement behavior at different curing times

4.1.1 Mode-I load-displacement curves under various displacement rates

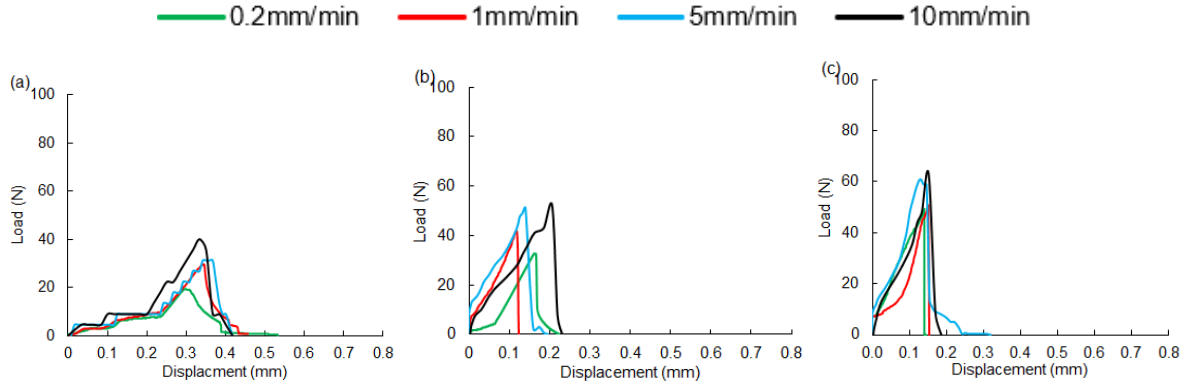

Figure 4.1. Mode-I load-displacement curves of control CPB under four displacement rates: (a) 7 days, (b) 28 days, and (c) 90 days.

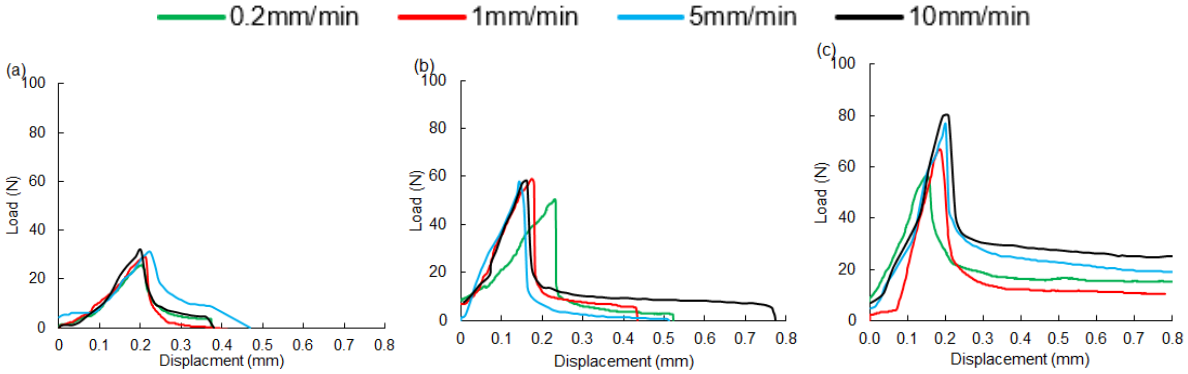

Figure 4.2. Mode-I load-displacement curves of FR-CPB (fiber length: 13mm and fiber content: 0.5%) with four displacement rates: (a) 7 days, (b) 28 days, and (c) 90 days.

Figures 4.1 and 4.2 show the load-displacement curves for CPB and FR-CPB at four displacement rates, respectively. The displacement rates changed from 0.2 to 10 mm/min and showed the load trend against displacement. At 7 days, the loading rates cause a relatively weak difference in the load-displacement curves. This can be interpreted by the

relatively weak matrix of early-age CPB. As a result, the tailing particle interaction can be governed by the pore water pressure. Therefore, the loading-rate dependency is not obvious at this stage. For the advanced-age (28 and 90 days) samples, the displacement rate can affect both pre-peak slopes and peak resistance loads. The slope of load-displacement curves gradually becomes similar in both CPB and FR-CPB. Under a higher displacement rate, FR-CPB demonstrates an enhanced peak resistance load under mode-I SCB tests. For instance, under 10mm/min at 90 days, there is a 22% increase in peak load when using fiber. Meanwhile, a higher displacement rate also results in a steeper slope of CPB and FR-CPB under mode-I SCB tests. The crack displacement is observed to be consistent across the curing time.

For the post-peak branch, a sudden drop of resistance consistently appears after the peak resistance load, and a high displacement rate can strengthen the rate of change in the resistance load. For control CPB (Figure 4.1), samples fracture in a brittle manner, and load resistance values suddenly drop to zero. However, after the sudden resistance drop, all FR-CPB demonstrate a stable residual resistance under various displacement rates (Figure 4.2). The corresponding residual resistance load can be enhanced as the displacement rate increases, consistent with the evolution of peak resistance under different displacement rates. At 90 days, the post-peak displacement in FR-CPB goes beyond 0.8mm, indicating the hardened CPB matrix's contribution to the fiber reinforcement effect during the post-peak stage. Therefore, the consistent existence of post-peak resistance can confirm the effectiveness of the fiber reinforcement technique under various displacement rates.

4.1.2 Mode-II load-displacement curves under various displacement rates

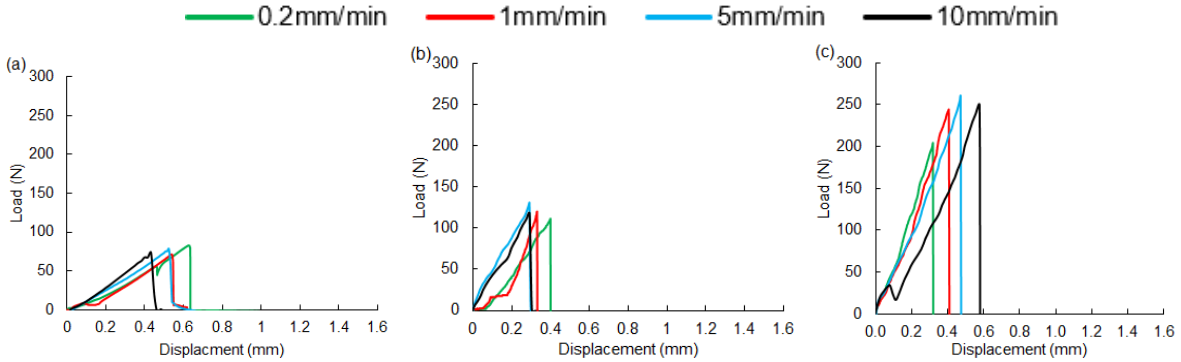

Figure 4.3. Mode-II load-displacement curves of control CPB with four displacement rates: (a) 7 days, (b) 28 days, and (c) 90 days.

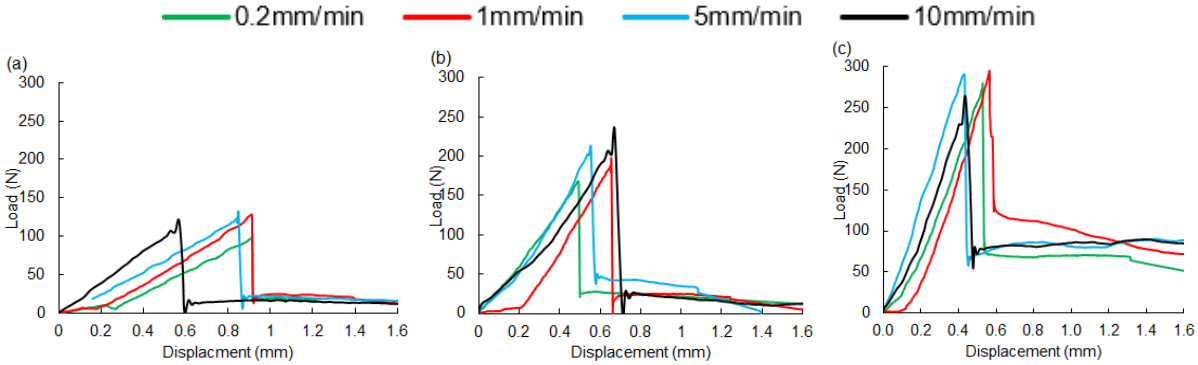

Figure 4.4. Mode-II load-displacement curves of FR-CPB (fiber length: 13mm and fiber content: 0.5%) with four displacement rates: (a) 7 days, (b) 28 days, and (c) 90 days.

The effect of displacement rates on the mode-II loading-displacement curves of control CPB and FR-CPB is shown in Figure 4.3 and Figure 4.4, respectively. It should be noted that compared with mode-I fracture behavior, mode-II fracture behavior also involves inter-particle friction resistance, which can mobilize along the shear crack surface and further contribute to the development of fracture resistance. More precisely, compared with the mode-I pre-peak branch, the discrepancy of the mode-II pre-peak branch becomes more obvious under various displacement rates, which indicates the dominant

role played by the CPB matrix. The peak load under mode-II loading is higher than measured under mode-I loading conditions. This suggests that shear stress is more vital than tensile stress and needs additional load to initiate a fracture. At the advanced ages, the peak load improves as the particle friction in the matrix is enhanced due to the consumption of pore water by binder hydration. Moreover, the sensitivity of mode-II peak load to the loading rates is weaker than the counterparts measured under the mode-I SCB test. For instance, under a displacement rate of 10mm/min at 90 days, there is an average peak load increase of 11% in FR-CPB, whereas the mode-I peak resistance increases by 24%. Moreover, the displacement corresponding to the peak load becomes smaller than those measured under low displacement rates.

Like mode-I load-displacement curves, control CPB samples under mode-II loading have the same post-peak with no residual resistance (Figure 4.3). In contrast, the FR-CPB mode-II post-peak branch consistently appears under various displacement rates, which indicates the effectiveness of fiber reinforcement at the mode-I post-peak stage. It is of great importance to note that the mode-II post-peak response shows a weaker sensitivity to the displacement rates relative to the counterparts measured under mode-I loadings. The finding further confirms that the CPB matrix dominates the pre-peak response and thus shows a higher-extern sensitivity to the displacement rates. At the same time, the post-peak behavior is governed by the reinforced fibers and demonstrates limited sensitivity to displacement rates. This scenario is extensively identified at FR-CPB at advanced ages. The post-peak resistance is highly marked and consistent between 50 N and 100 N.

4.1.3 Mode-III load-displacement curves under various displacement rates

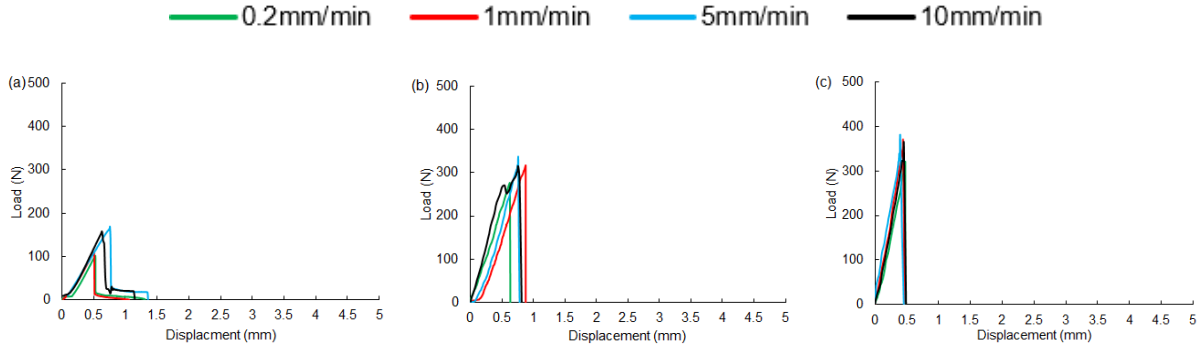

Figure 4.5. Mode-IIII load-displacement curves of control CPB with four displacement rates: (a) 7 days, (b) 28 days, and (c) 90 days.

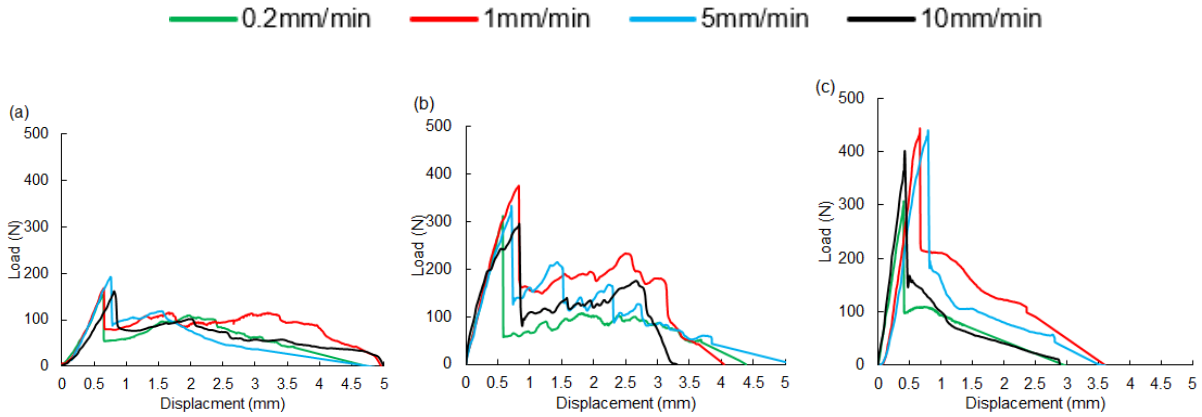

Figure 4.6. Mode-III load-displacement curves of FR-CPB (fiber length: 13mm and fiber content: 0.5%) with four displacement rates: (a) 7 days, (b) 28 days, and (c) 90 days.

Figures 4.5 and 4.6 illustrate the effect of displacement rates on the mode-III load-displacement curves of control CPB and FR-CPB, respectively. The mode-III pre-peak branches are similar to mode-II ones as they tend to have linear pre-peak slopes under various displacement rates, confirming the validity of linear elastic fracture mechanics to CPB materials. Since no cracks are considered at the pre-peak stage, the pre-peak response can be assumed to be governed by the intact CPB matrix. The consistent linear pre-peak response of both control CPB and FR-CPB implies the dominant role played by

the CPB matrix. Like mode-II behavior, the peak load shows sensitivity to the changes in loading rates. Specifically, the peak load increases until the loading rate reaches 5mm/min, followed by a reduction in peak load under a displacement rate of 10mm/min. Contrasting to mode-II, the higher displacement rates cause higher crack displacement values under mode-III loading conditions.

Similar to results measured under mode-II loading condition, there is no post-peak resistance of control CPB under mode-III loading (Figure 4.5). The mode-III post-peak behavior of FR-CPB is different from that observed under mode-II loading conditions, shown in Figure 4.6. A pseudo-hardening behavior (i.e., secondary peak load) is widely measured at the post-peak stage of FR-CPB under mode-III loading conditions. Compared with the mode-II post-peak response, the consistent appearance of pseudo-hardening behavior indicates distinct mechanisms for the post-peak response of FR-CPB under mode-II and mode-III loading conditions. The mode-II residual response is dominated by particle friction and fiber pull-out process. However, under mode-III loading conditions, the out-of-plane shear inevitably strengthens the fiber-matrix interaction and further leads to the edge-cutting process by the fibers. The enhanced fiber-matrix interaction definitely improves the post-peak resistance to the crack propagation and thus causes the pseudo-hardening behavior under mode-III loading conditions. In addition, mode-III load-displacement curves also demonstrate a sensitivity to the changes in the loading rates. For instance, at the 1mm/min displacement rate, there is a 57% and 17% increase in peak load between 7 to 28 days and 28 to 90 days, respectively. Therefore, mode-III is more sensitive to displacement rate at post-peak than pre-peak. Most

importantly, compared with the mode-II response, the post-peak response becomes more sensitive to the loading rates under mode-III loading conditions, which can be attributed to the strengthened matrix-fiber interaction under out-of-plane shear stress.

4.2 Effect of fiber length and fiber content on load-displacement curves of FR-CPB

4.2.1 Effect fiber length and fiber content on the mode-I load-displacement curves of FR-CPB under various loading rates

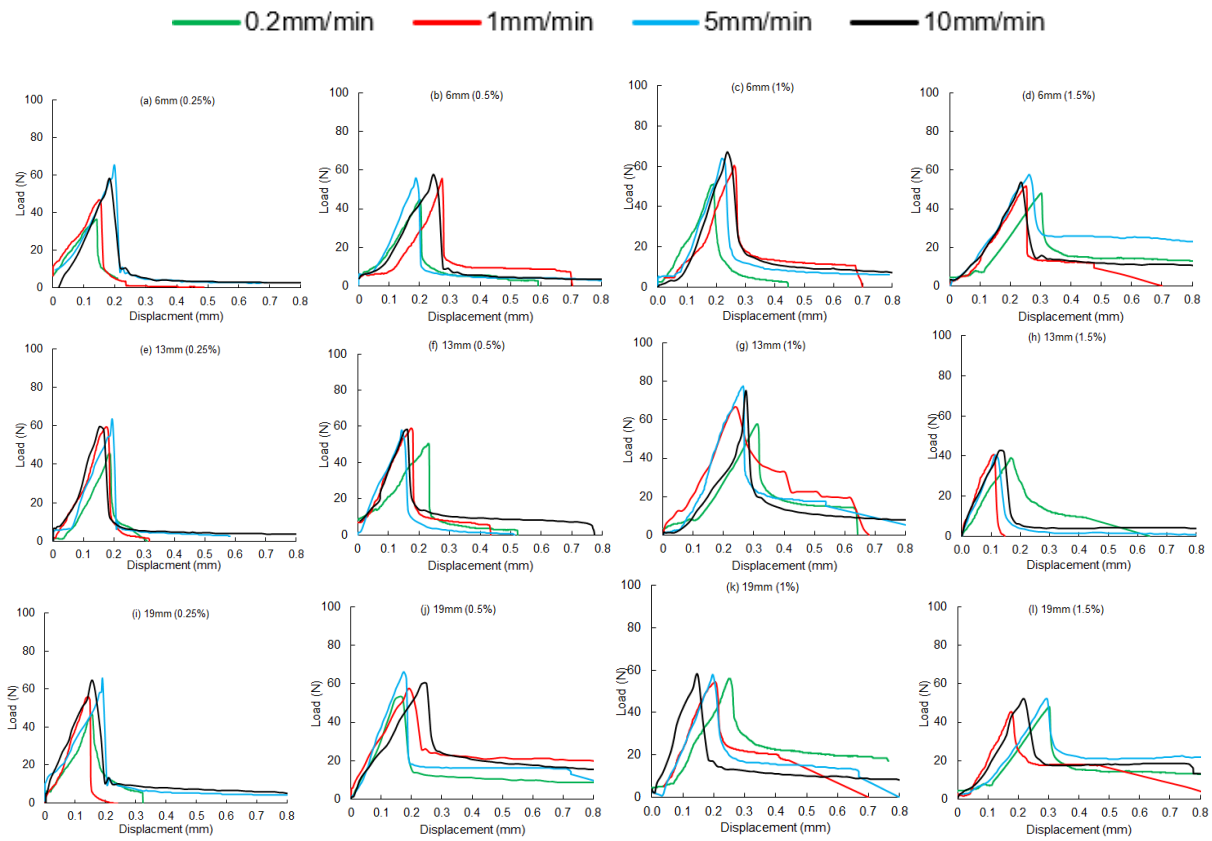

Figure 4.7. Mode-I load-displacement curves of FR-CPB at four displacement rates at 28 days: (a) 6mm and 0.25% (b) 6mm and 0.5% (c) 6mm and 1% (d) 6mm and 1.5% (e) 13mm and 0.25% (f) 13mm and 0.5% (g) 13mm and 1% (h) 13mm and 1.5% (i) 19mm and 0.25% (j) 19mm and 0.5% (k) 19mm and 1% (l) 19mm and 1.5%.

Figure 4.7 shows the effect of fiber length and fiber content on the mode-I load-displacement curves under various loading rates. The effect of fiber length and content on the mode-I curves differs. First, it can be observed that the changes in fiber length and fiber content do not influence the pre-peak linear response under various displacement rates, i.e., adding fibers does not change the pre-peak linear behavior of CPB, which indicates the dominant role played by the CPB matrix. Therefore, adding fibers does not undermine the validity of linear elastic fracture mechanics to the pre-peak response of FR-CPB. Moreover, the peak load appears between 0.1mm and 0.2mm, which suggests the crack is taking place due to the loss of resistance and brittle property of the CPB matrix. Peak resistance load changes under various displacement rates, and FR-CPB demonstrates a more significant peak resistance load under a higher displacement rate. Compared to the curves of CPB (Figure 4.1.b), there is an increase in peak load in FR-CPB samples. The peak load consistently increases up to fiber content of 1% and then decreases as fiber content further increases to 1.5%. This is because a competing effect of fiber reinforcement exists in the CPB matrix. First, the increase in fiber content tends to increase the reinforcement effect on the matrix. Second, the excessive usage of fibers unavoidably interferes with the tailing particle packing and thus leads to a negative influence on the matrix integrity, i.e., matrix degradation. Consequently, a degraded response can be observed at a high fiber content.

Moreover, FR-CPB shows a relatively stable post-peak residual resistance under different displacement rates, indicating the fibers' reliable bridging effect in the CPB matrix under mode-I loading conditions. FR-CPB samples with 0.25% low resistance showed behavior

similar to that measured from control CPB. There is a better resistance for FR-CPB with a fiber length of 19mm, but still not adequate (Figure 4.7.i). FR-CPB demonstrates the sensitivity of post-peak resistance, mainly from FR-CPB, with fiber contents of 0.5% and 1%. When fiber contents reach 0.5% and 1%, an enhanced post-peak resistance can be expected as the fiber length increases. However, when excessive fibers were adopted, i.e., 1.5% fiber content, a lower post-peak resistance appeared.

4.2.2 Effect fiber length and fiber content on the mode-II load-displacement curves of FR-CPB under various loading rates

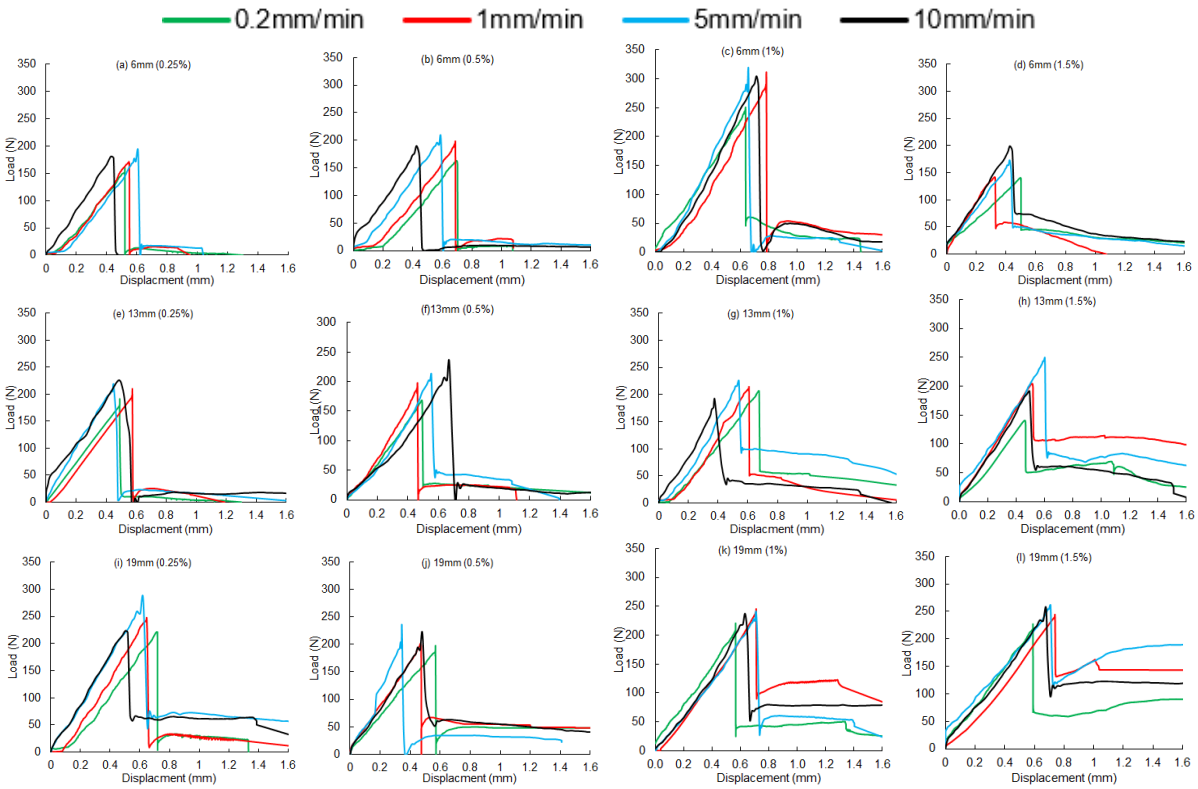

Figure 4.8. Mode-II load-displacement curves of FR-CPB at four displacement rates at 28 days: (a) 6mm and 0.25% (b) 6mm and 0.5% (c) 6mm and 1% (d) 6mm and 1.5% (e) 13mm and 0.25% (f) 13mm and 0.5% (g) 13mm and 1% (h) 13mm and 1.5% (i) 19mm and 0.25% (j) 19mm and 0.5% (k) 19mm and 1% (l) 19mm and 1.5%.

As shown in Figure 4.8, a linear pre-peak branch is observed under mode-II loading, which is similar to the mode-I pre-peak response. Meanwhile, the displacements corresponding to the peak load differ from one another, depending on the fiber content and displacement rates. This is because the amount of fiber in the sample has a limited effect on shear resistance as the load is mainly concentrated locally (around the notch). The shorter fiber length has a better peak-load value and linear slope. Moreover, the 5mm/min yields a higher peak-load value of FR-CPB under mode-II loading.

Compared with mode-I post-peak behavior, FR-CPB shows a sharp recovery in post-peak resistance immediately following the sudden drop in peak load. It should be pointed out that a sliding displacement between shear cracks is required to activate the bridging effect after initiating mode-II shear cracks. Before the activation of the bridging effect takes place, FR-CPB is still dominated by its matrix and thus shows a sudden drop in peak load. After the activation of the bridging effect, a stronger reinforcement appears and can maintain the post-peak resistance. As illustrated in Figure 4.8, mode-II post-peak behavior becomes sensitive to displacement rates at a high fiber content (1% and 1.5%) and a longer fiber length (19mm). The usage of such fiber parameters improves the drop after crack as the high amount of fiber in the matrix recovers to resist the load.

4.2.3 Effect fiber length and fiber content on the mode-III load-displacement curves of FR-CPB under various loading rates

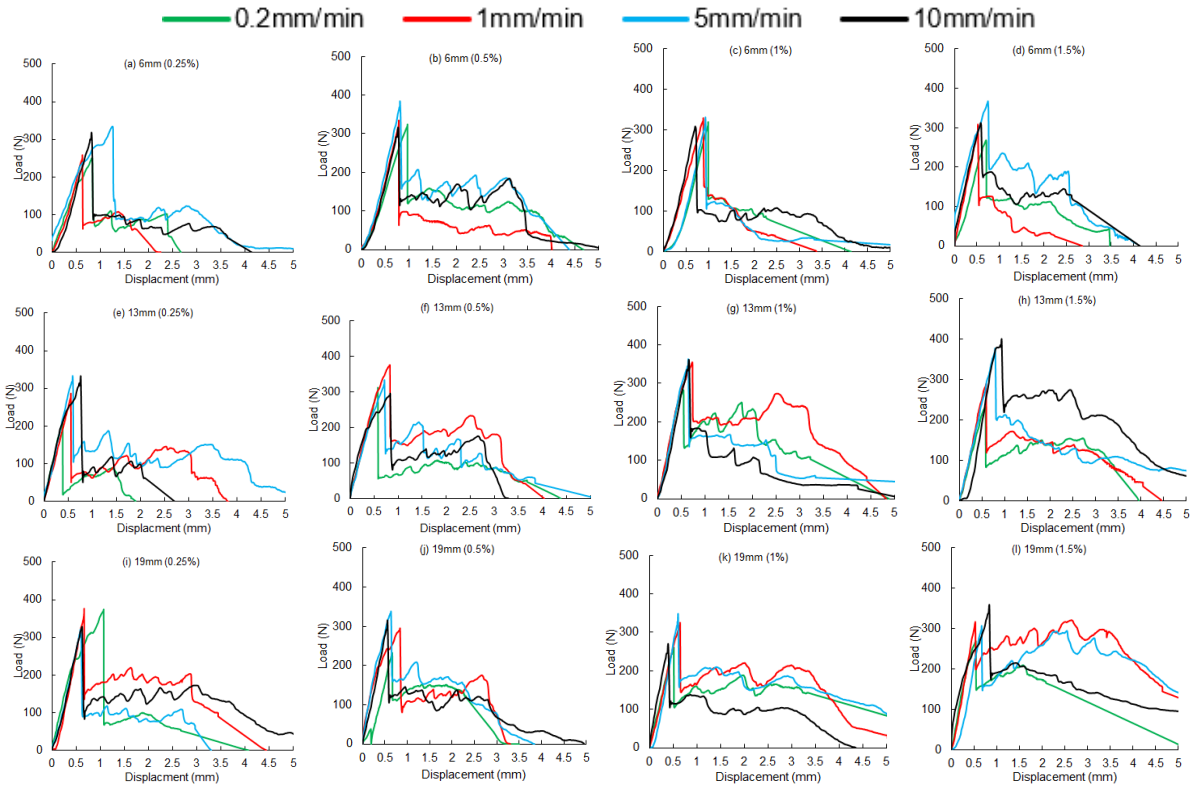

Figure 4.9. Mode-III load-displacement curves of FR-CPB at four displacement rates at 28 days: (a) 6mm and 0.25% (b) 6mm and 0.5% (c) 6mm and 1% (d) 6mm and 1.5% (e) 13mm and 0.25% (f) 13mm and 0.5% (g) 13mm and 1% (h) 13mm and 1.5% (i) 19mm and 0.25% (j) 19mm and 0.5% (k) 19mm and 1% (l) 19mm and 1.5%.

Figure 4.9 demonstrates the effect of fiber length and fiber content on the mode-III load-displacement curves of FR-CPB under various displacement rates. It can be observed that the pre-peak response of mode-III curves remains linear changes, the same as in mode-II pre-peak branches. However, unlike mode-II behavior, the peak load is higher under mode-III loading. Moreover, FR-CPB also shows similar pre-peak slopes under various displacement rates. This is because the load is mainly carried by the CPB matrix

rather than the fibers at the pre-peak stage. The improvement of peak load depends on fiber length and content. A monotonic increase in the peak load is measured from FR-CPB with a fiber content of up to 1%. For the influence of fiber length, the 13mm fiber length produces a higher peak load. Similar to the results under mode-II loading, the 5mm/min displacement rate causes a higher peak load, while a higher displacement rate (10mm/min) leads to a reduction in the peak load.

Compared with mode-II post-peak behavior, FR-CPB illustrates a pseudo-hardening behavior. Moreover, it is interesting to observe that a more substantial fluctuation of post-peak resistance appears before the second post-peak, followed by a relatively smooth drop in post-peak resistance. This energy drop becomes smaller with the increase in fiber content. The fluctuation of post-peak resistance can be attributed to the solid out-of-plane crack interaction. FR-CPB shows a consistent sensitivity of post-peak resistance to displacement rates, confirming the matrix's dominant role under mode-III loading conditions. Moreover, the lower displacement rates result in a higher resistance at post-peak and higher displacement at 13mm and 19mm fiber lengths.

4.3 Effect of displacement rates on fracture toughness of FR-CPB

4.3.1 Mode-I fracture toughness under various displacement rates

Figure 4.10 represents the mode-I fracture toughness of FR-CPB with three fiber lengths and five fiber contents under different displacement rates. It can be observed that mode-I fracture toughness is sensitive to the displacement rate and shows an increasing trend as it increases. More specifically, when the displacement rate is increased from 0.2

mm/min to 1 mm/min, FR-CPB and control CPB consistently demonstrate a considerable improvement in fracture toughness from early to advanced ages. As the displacement rate further increases, the rate of improvement in fracture toughness becomes weaker. For instance, in Figure 4.10.g, there is a 10% increase between 0.2 to 1 mm/min and 5.4% between 1 to 10 mm/min. Meanwhile, the curing time can influence the sensitivity of fracture toughness to the displacement rates. Compared with the 7 days and 28 days measured results, 90 days FR-CPB demonstrates a higher-extent discrepancy of fracture toughness as the displacement rates increase. This can be attributed to the hardened CPB matrix and inter-bonding of fiber with cement at 90 days, which can offer more vital tailings particle interaction (Figure 4.11.c and 4.12.c). For a given quantity of cement, the amount of water combined in ettringite crystals is higher than in other hydrates. The capacity of ettringite is 85%, meaning that 100 g of anhydrous phases can combine 85 g of water within the crystallized network of ettringite. As a comparison, the capacity of gypsum is only 27%, whereas it is around 30% for C-S-H [Peter et al., 2019]. Therefore, the loading-rate dependency becomes more evident at the advanced age. Moreover, it is also interesting to observe that the influence of fiber inclusion mainly occurs at 90 days, while the fracture toughness of CPB with the various fiber lengths and fiber content shows similar evolutionary trends and magnitudes at 7 and 28 days. Most importantly, it can be observed that compared with fiber content, changes in fiber length lead to the loading-rate sensitivity of mode-I fracture toughness to a greater extent. Using a short fiber length causes a more obvious discrepancy in loading-rate dependency in fracture toughness. This is because when fiber content is fixed, introducing shorter fibers into the CPB matrix

increases the number of fibers locally. Correspondingly, shorter fiber can influence the formation of microstructure to a greater extent via its influence on the tailing particle packing, thereby interfering with the displacement-rate-dependent fracture toughness at the macroscale.

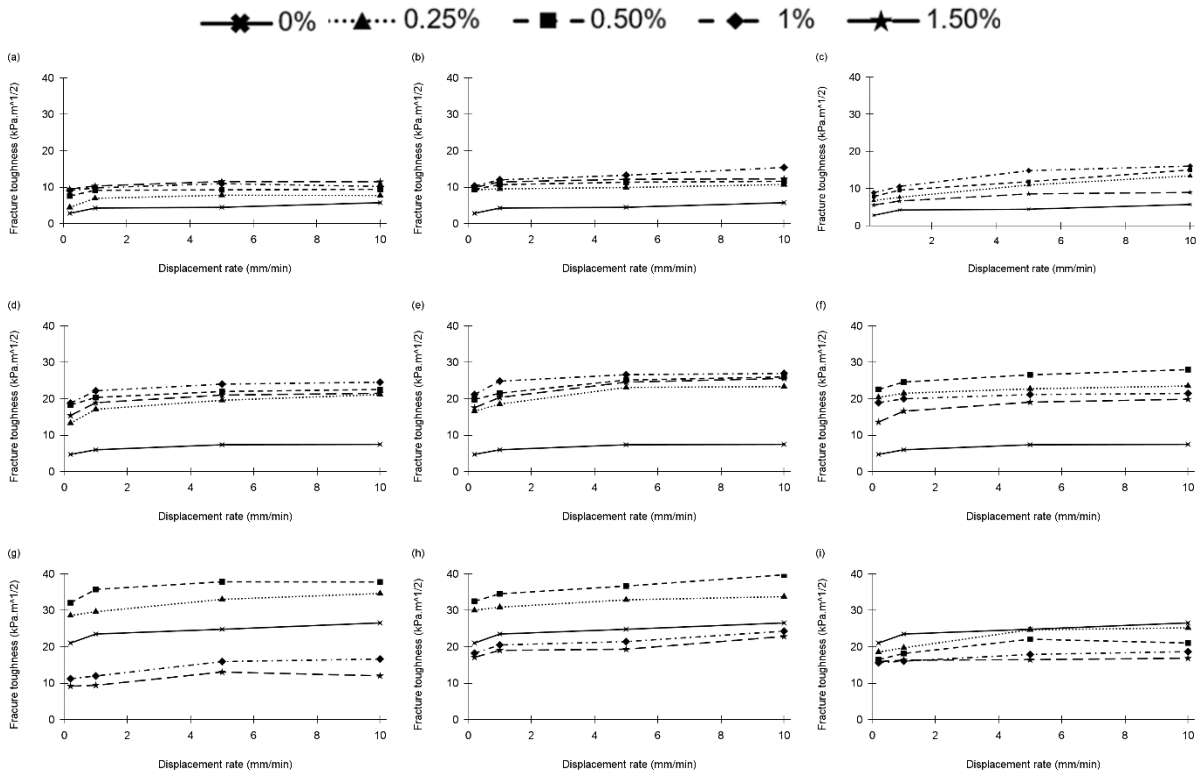

Figure 4.10. Effect of PP fiber on mode-I fracture toughness under various displacement rates: (a) 6mm at 7 days, (b) 13mm at 7 days, (c) 19mm at 7 days, (d) 6mm at 28 days, (e) 13mm at 28 days, (f) 19mm at 28 days, (g) 6mm at 90 days, (h) 13mm at 90 days, and (i) 19mm at 90 days.

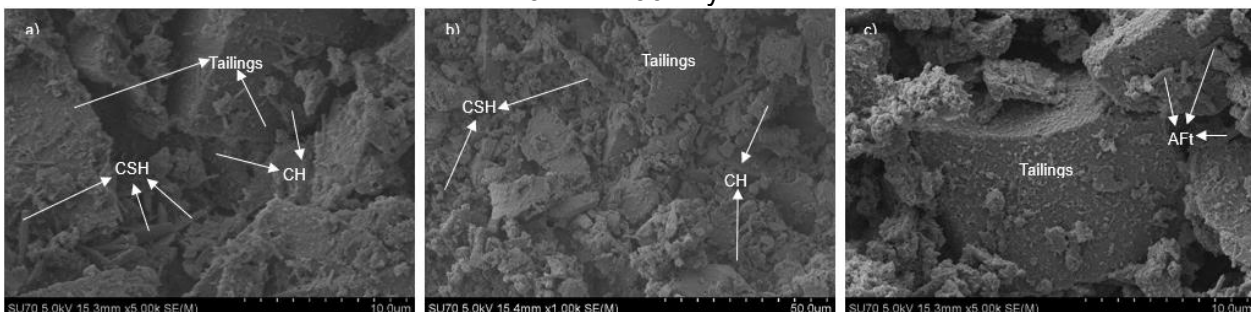

Figure 4.11. SEM images of CPB at three curing times: (a)7 days, (b) 28 days, and (c) 90 days.

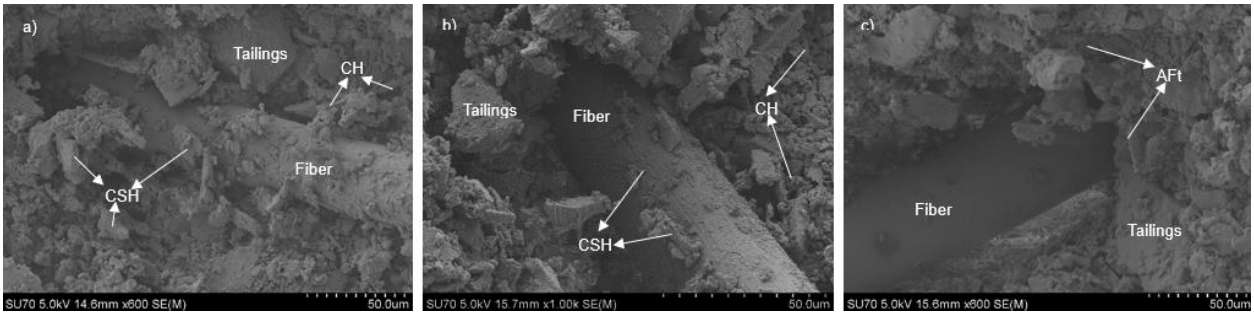

Figure 4.12. SEM images of FR-CPB at three curing times: (a)7 days, (b) 28 days, and (c) 90 days.

Besides the influence of displacement rate on fracture toughness, the magnitude of mode-I fracture toughness also demonstrated a stronger dependency on fiber inclusion. As shown in Figure 4.10, FR-CPB shows consistently higher fracture toughness than the counterparts measured from the CPB at 7 and 28 days. Moreover, increased fiber length and content persistently enhance the 7-day fracture toughness. When the curing time reaches 28, the optimal fiber content changes to 1% (corresponding to the fiber lengths of 6mm and 13mm) and 0.5% (corresponding to the fiber length of 19mm), which can yield a maximum fracture toughness of FR-CPB. In other words, the obtained results indicate that using excessive fibers can weaken the integrity of the CPB matrix and thus lead to a relative degradation of fracture toughness. Such an evolutionary trend becomes more evident from 90 days of fracture toughness. Figure 4.10 (g-i) shows that the reinforcement effect on mode-I fracture toughness was only observed from FR-CPB with fiber lengths of 6mm and 13mm and fiber content of 0.25% and 0.5% at 90 days. Using 19-mm fibers leads to the degradation of fracture toughness compared to the control CPB. Regarding fiber content, a weakened fracture toughness appears in FR-CPB as the

fiber content increases to 1% and 1.5%. Therefore, the measured results reveal the existence of optimal fiber parameters for applying fiber reinforcement technique in the mine backfill design.

4.3.2 Mode-II fracture toughness under various displacement rates

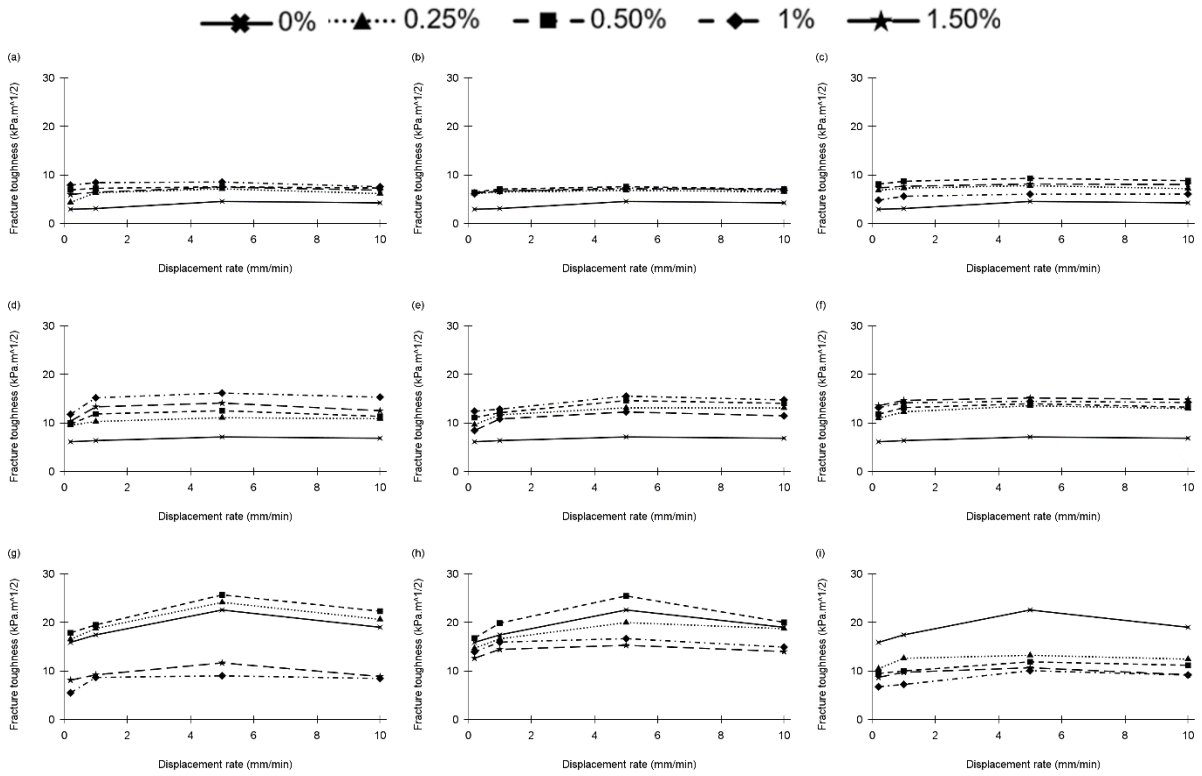

Figure 4.13. Effect of PP fiber on mode-II fracture toughness under various displacement rates: (a) 6mm at 7 days, (b) 13mm at 7 days, (c) 19mm at 7 days, (d) 6mm at 28 days, (e) 13mm at 28 days, (f) 19mm at 28 days, (g) 6mm at 90 days, (h) 13mm at 90 days, and (i) 19mm at 90 days.

Apart from the identification of the dependence of mode-II fracture toughness on displacement rate, it is also necessary to reveal the influence of fiber length and fiber content on mode-II fracture toughness. As shown in Figure 4.13 (a-c), the increase in fiber content promotes the development of mode-II fracture toughness, where the effect

of fiber length is negligible. The increase of fiber content up to 1.5% showed a decrease in fracture toughness at early ages. At 28 days, FR-CPB with 1% fiber content shows a higher mode-II fracture toughness, especially for those prepared with 6mm and 13mm fibers. For instance, Figure 4.13.d shows a 50% increase in fracture toughness with a rise in fiber content from 0.25% to 1%. Higher fiber content showed no improvement in maintaining crack propagation. At advanced ages, the effect resulting from the increase in fiber length is negligible. At 90 days, the fracture toughness is more affected by fiber content rather than the fiber length. As shown in Figure 4.13 (g-i), the reinforcement effect of mode II fracture toughness was only observed from FR-CPB with fiber lengths of 6mm and 13mm and a fiber content of 0.5%. Using 19mm fibers results in a lower mode-II fracture toughness, which was not comparable to that from control CPB. Therefore, mode-II fracture toughness is more influenced by fiber content rather than fiber length.

4.3.3 Mode-III fracture toughness under various displacement rates

As shown in Figure 4.14, the evolutionary trend of mode-III fracture toughness is similar to those obtained under mode-II loading conditions. However, the critical displacement rate under mode-III loading is 1mm/min, which dramatically alters the rate of change in mode-III fracture toughness. More precisely, a sharp increase in mode-III fracture toughness was observed when the displacement rates increased from 0.2mm/min to 1mm/min. As the displacement further increases (up to 10 mm/min), the rate of change in mode-III fracture toughness becomes smaller. At 7 days, the sensitivity of fracture toughness to displacement rate is governed in a specific range, as shown in Figure 4.14 (a-c). In advanced days, the sensitivity of fracture toughness became clear in FR-CPB

samples. At 28 days, the fracture toughness at a higher displacement rate started losing its sensitivity, as shown in Figure 4.14 (d-f). This is governed by local damage and depreciation of water pressure at a notch. At 90 days, considering dry samples and unique micro-structure, the fracture toughness is observed to be sensitive to displacement rate. The 5mm/min results in higher fracture toughness (see Figure 4.14.g) than 1mm/min at the lower fiber content.

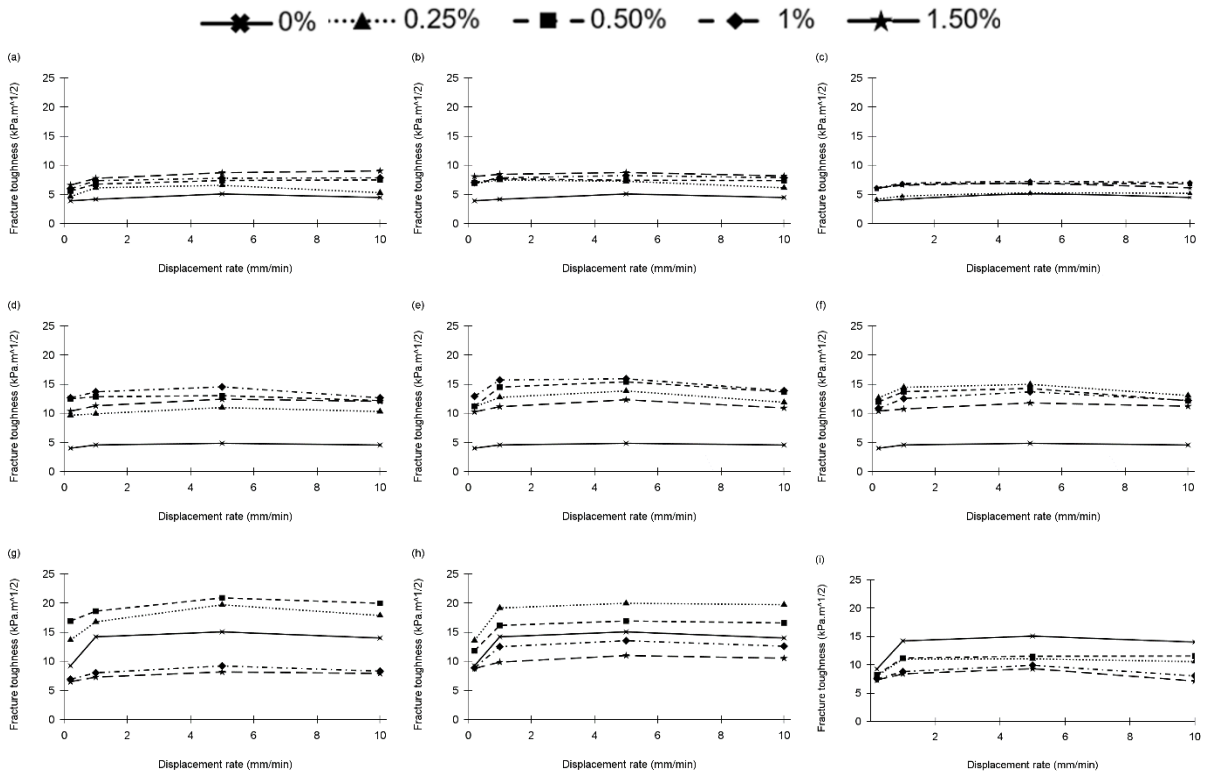

Figure 4.14. Effect of PP fiber on mode-II fracture toughness under various displacement rates: (a) 6mm at 7 days, (b) 13mm at 7 days, (c) 19mm at 7 days, (d) 6mm at 28 days, (e) 13mm at 28 days, (f) 19mm at 28 days, (g) 6mm at 90 days, (h) 13mm at 90 days, and (i) 19mm at 90 days.

Regarding the influence of fiber length and fiber content, the increase in fiber content shows an enhancement in fracture toughness at 7 days. However, there is limited variation when doubling the fiber length. At 28 days, the FR-CPB samples started to show

the effect of fiber content and length. It can be observed that the fiber content of 1% can be considered an optimum fiber content across three fiber lengths. For instance, fiber content higher than 1% showed a drop of 40% in the mode-III fracture toughness. Moreover, 13mm (1.5%) fiber was 17% less value than 13mm (0.25%). At 19mm fiber length, 0.25% was observed to have a higher fracture toughness, shown in Figure 4.14.f. At 90 days, the fracture toughness is more affected by fiber content other than the fiber length. The FR-CPB samples with 1% and 1.5% fiber contents showed lower fracture toughness than control samples, shown in Figure 4.14 (g-i). The same results were obtained from the mode-II loading condition, where 19mm fiber length leads to a lower fracture toughness than control samples. Therefore, using 13mm fibers can maximize the fiber reinforcement effect on the mode-III fracture toughness, while longer fibers had limited bonding structures with the matrix. This phenomenon increases weak zones in the matrix structure and initiates crack propagation.

4.4 Effect of displacement rates on stiffness

4.4.1 Mode-I stiffness under various displacement rates

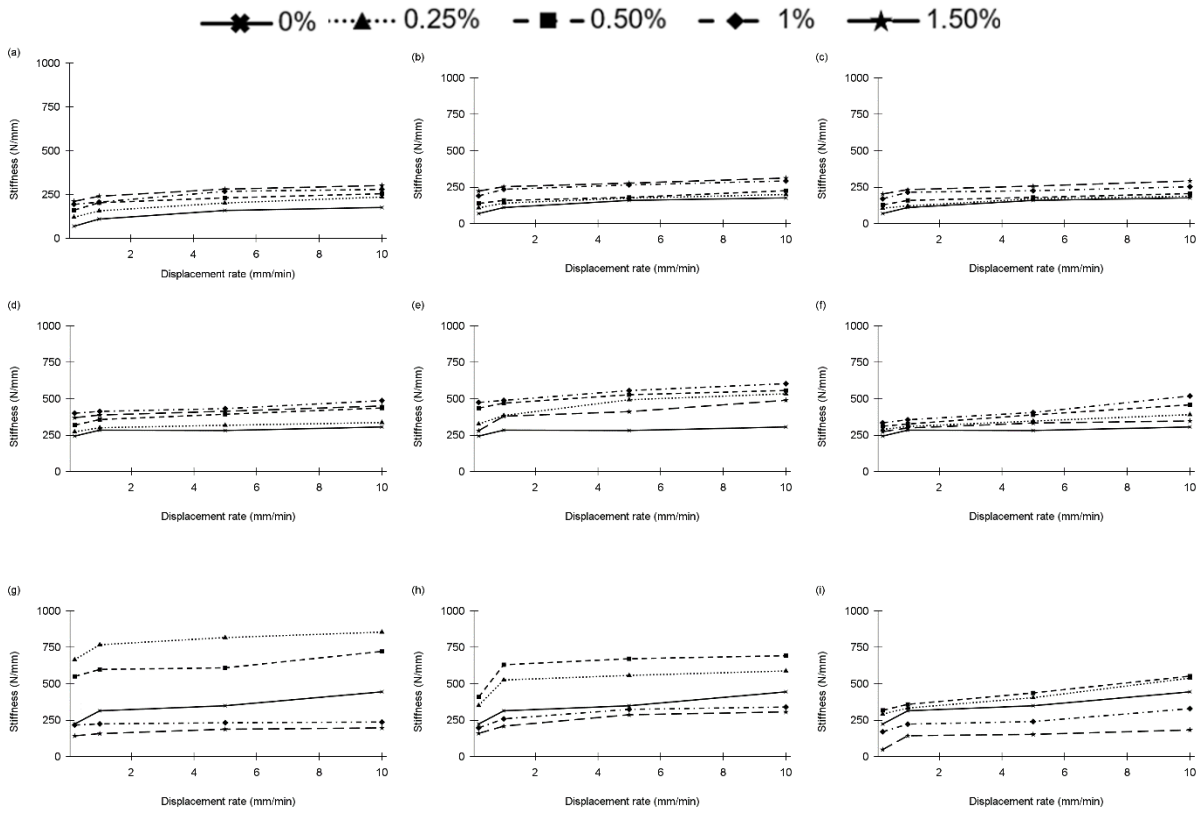

Figure 4.15. Effect of PP fiber on mode-I stiffness under various displacement rates: (a) 6mm at 7 days, (b) 13mm at 7 days, (c) 19mm at 7 days, (d) 6mm at 28 days, (e) 13mm at 28 days, (f) 19mm at 28 days, (g) 6mm at 90 days, (h) 13mm at 90 days, and (i) 19mm at 90 days.

At 7 and 28 days, the discrepancy of stiffness with different fiber content is minimal, and it continuously increases with improvement in fiber content. Meanwhile, 90 days of FR-CPB demonstrates an apparent change in displacement-rate-dependent stiffness with different fiber content. Low cement content (Cc=4.5%) and high water content (WTR=0.36) lead to a relatively soft matrix at 7 and 28 days. Correspondingly, the interface bonding strength between fibers and tailings is inevitably weak, and including

fibers results in no critical influence on the matrix integrity. Consequently, the 7 and 28 days FR-CPB samples show similar changes in stiffness as the fiber content changes. However, as shown in Figure 4.15, it can be observed that 90 days of FR-CPB shows a more substantial stiffness disparity under different fiber content. This is due to the combined effect of continuous cement hydration and the development of matrix suction in the interfacial transition zone between tailings and fibers. As a result, the interfacial bonding strength can be significantly enhanced and thus positively contribute to the matrix stiffness. At 90 days stiffness, there is a reduction when fiber content is more significant than 0.5% compared with the counterpart of control CPB. The stiffness degradation can be attributed to the deterioration effect of fiber inclusion on the matrix integrity. As discussed before, the CPB matrix plays a dominant role in the development of material stiffness. As more fibers are introduced into the matrix, the excessive fibers unavoidably impede the tailing particles packing densely via the wall effect in the interfacial transition zone. Therefore, the matrix integrity degradation will occur when the fiber content passes its critical value, i.e., 0.5% in the present study. The obtained critical fiber content also indicates a competing effect in the development of stiffness, i.e., the fiber reinforcement and fiber-induced matrix degradation. Like the influence of fiber content, fiber length leads to minimal changes in 7 and 28 days stiffness under various displacement rates. However, short fiber can lead to a higher extent of discrepancy of stiffness at 90 days. For example, compared with using 6mm fibers (Figure 4.15.g), the stiffness of FR-CPB with 13mm and 19mm fibers becomes closer to that of the control sample. This is because the number of fibers reduces locally as the fiber length increases. Hence, the data

disparity relevant to the control sample becomes weaker. Based on the obtained results from the present study, it is highly recommended that the critical fiber content and length be integrated into the optimal design of FR-CPB in practice, which has the potential to maximize the mechanical and economic performance of fiber reinforcement in mine backfill technology.

4.4.2 Mode-II stiffness under various displacement rates

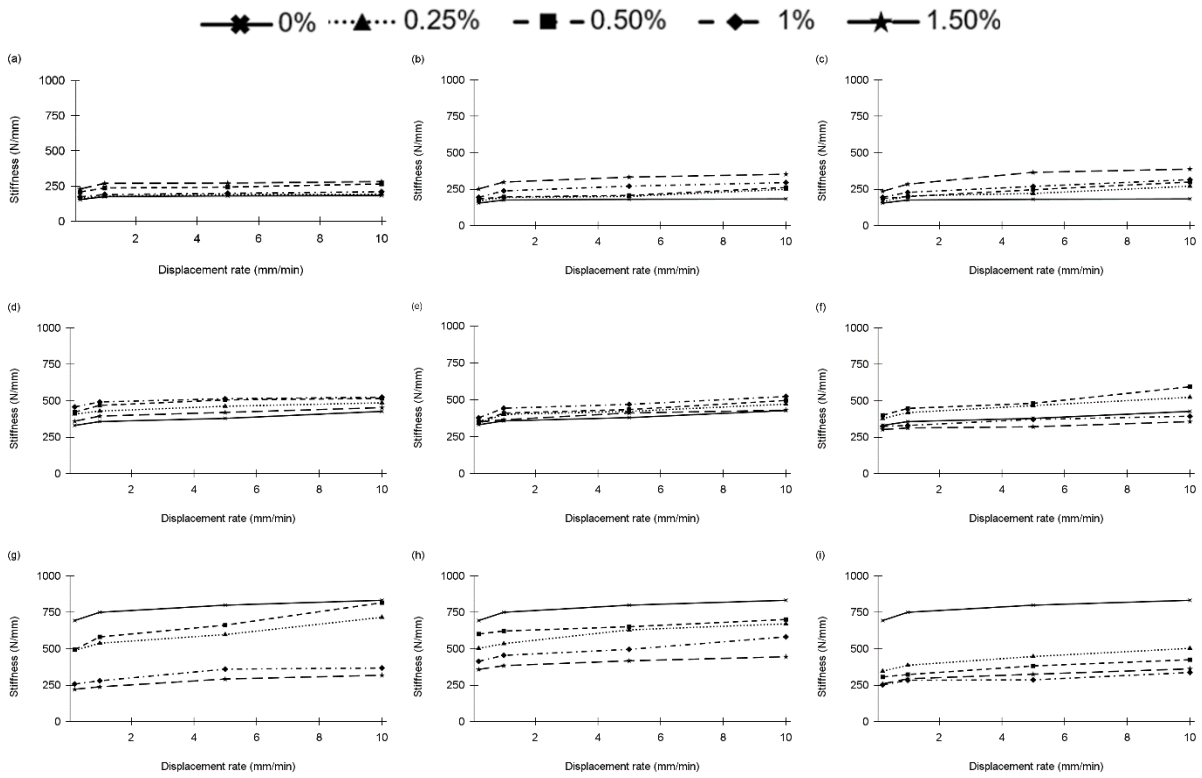

Figure 4.16. Effect of PP fiber on mode-II stiffness under various displacement rates: (a) 6mm at 7 days, (b) 13mm at 7 days, (c) 19mm at 7 days, (d) 6mm at 28 days, (e) 13mm at 28 days, (f) 19mm at 28 days, (g) 6mm at 90 days, (h) 13mm at 90 days, and (i) 19mm at 90 days.

The evolution of mode-II stiffness under various displacement rates is plotted in Figure 4.16. It can be seen that FR-CPB and CPB stiffness under mode-II loading have a similar trend with the increase in displacement rate. Like mode-I stiffness, mode-II stiffness is more sensitive to a lower displacement rate at early ages. The critical displacement rate is identified to be 1mm/min, and a decrease in stiffness was observed at a higher displacement rate. This is due to the higher deformation of the matrix. At 90 days, the stiffness of FR-CPB with shorter fiber showed more sensitivity to displacement rate, which is the same as mode-I stiffness (Figure 4.16 (g-i)).

At 7 days, the improvement in mode-II stiffness is monotonic with increased fiber content. Also, it is sensitive to displacement rate when the fiber length increases. At 28 days, a higher fiber content causes a lower stiffness than that measured from FR-CPB with a lower fiber content. As shown in Figure 4.16.f, 1% and 1.5% fiber content can result in smaller stiffness than the control CPB. Similar to mode-I stiffness, fiber length makes a relatively limited contribution to the development of mode-II stiffness. However, it is observed that mode-II stiffness decreases by 10% with a change in fiber length from 6mm to 19mm. This is due to the local fiber degradation (Figure 4.16 (d-f)). Also, fiber inclusions can adversely affect the particle package and interlocking during shear stress. Compared with mode-I stiffness, the package and interlocking structure are more important to resist shear stress. At 90 days, the control CPB samples consistently showed higher stiffness across all fiber lengths. This indicates that the matrix dominates the formation of mode-II stiffness at advanced ages. Lower fiber content (0.25% and 0.5%) produces a stiffer FR-CPB, whereas more fibers in FR-CPB didn’t enhance the stiffness. For instance, as

shown in Figure 4.16.i, the 0.25% fiber content stiffness became critical, suggesting that the fiber doesn't improve stiffness.

4.4.3 Mode-III stiffness under various displacement rates

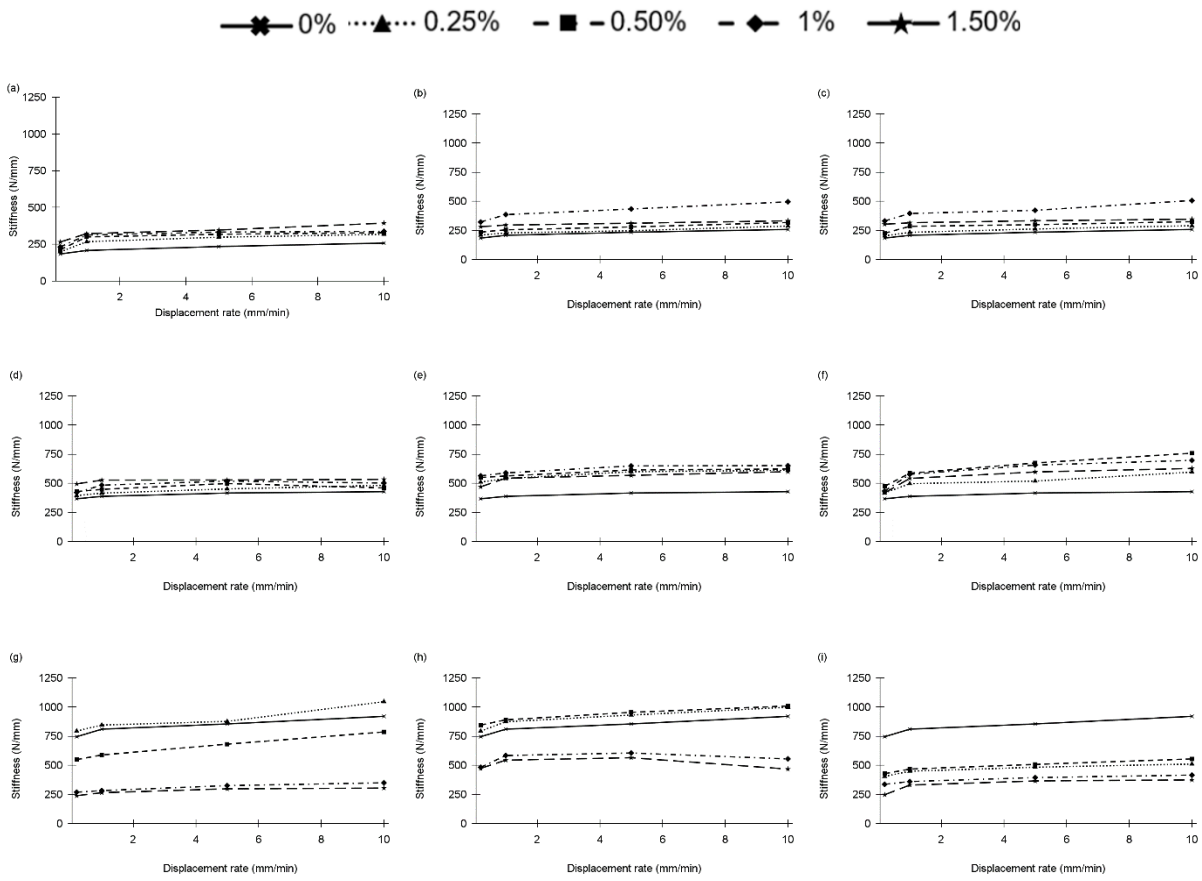

Figure 4.17. Effect of PP fiber on mode-III stiffness under various displacement rates: (a) 6mm at 7 days, (b) 13mm at 7 days, (c) 19mm at 7 days, (d) 6mm at 28 days, (e) 13mm at 28 days, (f) 19mm at 28 days, (g) 6mm at 90 days, (h) 13mm at 90 days, and (i) 19mm at 90 days.

From Figure 4.17, it can be observed that early-age mode-III stiffness is not sensitive to the change in displacement rates. As already discussed, the matrix is the dominant component for the development of stiffness. , The mode-III stiffness of FR-CPB shows a similar trend to that measured from the control samples. At 28 days, the stiffness of FR-

CPB improved and became sensitive to displacement rates. The sensitivity increases gradually at advanced ages, where the critical displacement rate stays at 1mm/min with the highest stiffness improvement. Moreover, the stiffness of mode-II and mode-III are comparable at 7 and 28 days. At 90 days, shorter fiber can yield a stronger stiffness sensitivity to displacement rates, also observed from changes in mode-II stiffness under various displacement rates.

At 7 days, 1% fiber content increases stiffness across all fiber lengths. The sensitivity of stiffness gradually improved with the increase in fiber length. At 28 days, the fiber content changed dramatically with the change in fiber length. Fiber lengths of 6mm, 13mm, and 19mm showed stiffness degradation with different critical fiber content, 1.5%, 1%, and 0.5%, respectively. At 90 days mode-III stiffness (Figure 4.17 (g-h)), 6mm and 13mm fibers can still positively contribute to the stiffness of FR-CPB with a lower fiber content (0.25% and 0.5%). Higher fiber content and length result in limited improvement in stiffness at advanced ages. The difference between mode-II and mode-III stiffness indicates the existence of an extra contributor to the formation of stiffness under mode-III loading conditions. Specifically, the out-of-plane shear stress can result in the torsion of crack surfaces relative to the crack front, thus inducing extra resistance from the matrix. The additional resistance caused by mode-III shear stress can positively contribute to the material stiffness. However, this aspect is not visible in FR-CPB with 19mm fiber length due to lower stiffness values than control CPB.

4.5 Effect of displacement rates on the crack initiation energy

4.5.1 Mode-I crack initiation energy under various displacement rates

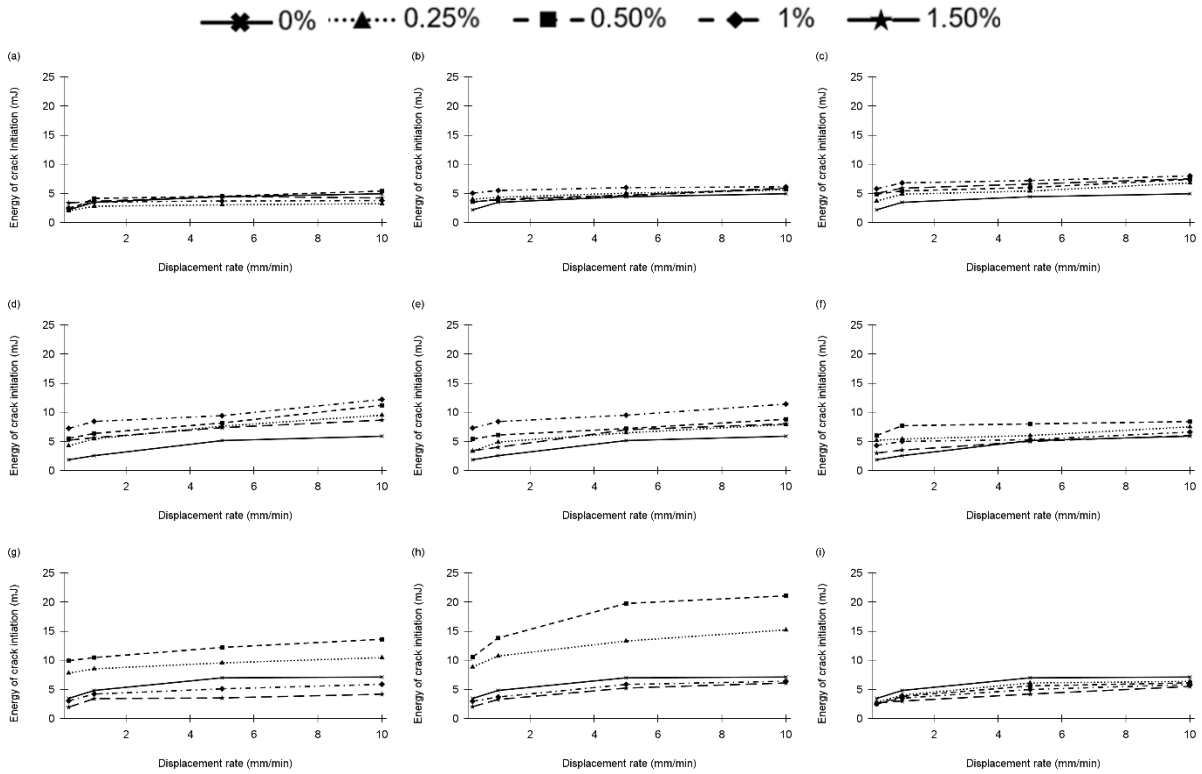

Figure 4.18. Effect of PP fiber in mode-I crack initiation energy under various displacement rates: (a) 6mm at 7 days, (b) 13mm at 7 days, (c) 19mm at 7 days, (d) 6mm at 28 days, (e) 13mm at 28 days, (f) 19mm at 28 days, (g) 6mm at 90 days, (h) 13mm at 90 days, and (i) 19mm at 90 days.

Figure 4.18 shows the trend of crack initiation energy under various displacement rates. At 7 days, the sensitivity of crack initiation energy of CPB and FR-CPB toward displacement rates is limited, the same as stiffness. The lower peak load and early age of the sample, resulting in the sample's low stability, limits the crack energy. As shown in Figure 4.18, the CPB and FR-CPB have similar trends with the increase of displacement rate at different curing times. This is due to the limited effect of fibers on initiating cracks in the samples, as 98% of the FR-CPB matrix are tailings, which governs the development

of macroscale fracture properties. Fiber is primarily beneficial for holding crack propagation through its bridging effect. At advanced ages, the sensitivity of crack initiation energy increased and showed a monotonic increase up until 5mm/min. However, a further increase in the displacement rate leads to a reduction in the crack initiation energy of FR-CPB.

At 7 days, crack initiation energy is in the range of 3mJ and 6mJ across all fiber lengths. The 1% and 0.5% fiber content result in the highest crack initiation energy at 28 and 90 days, respectively. At 28 days, increased fiber length can only cause limited sensitivity to higher displacement rates. At 90 days, improvement of crack initiation energy is only seen from FR-CPB with 6mm and 13mm fiber lengths and low fiber content (0.25% and 0.5%). At 19mm, control CPB shows a larger crack initiation energy and low fiber content leads to comparatively better results than higher ones (Figure 4.18.i). The degradation of crack initiation energy at higher fiber content is due to the weak interaction between fiber and matrix. Therefore, the influence of fibers is limited and restricted to resist crack propagation.

4.5.2 Mode-II crack initiation energy under various displacement rates

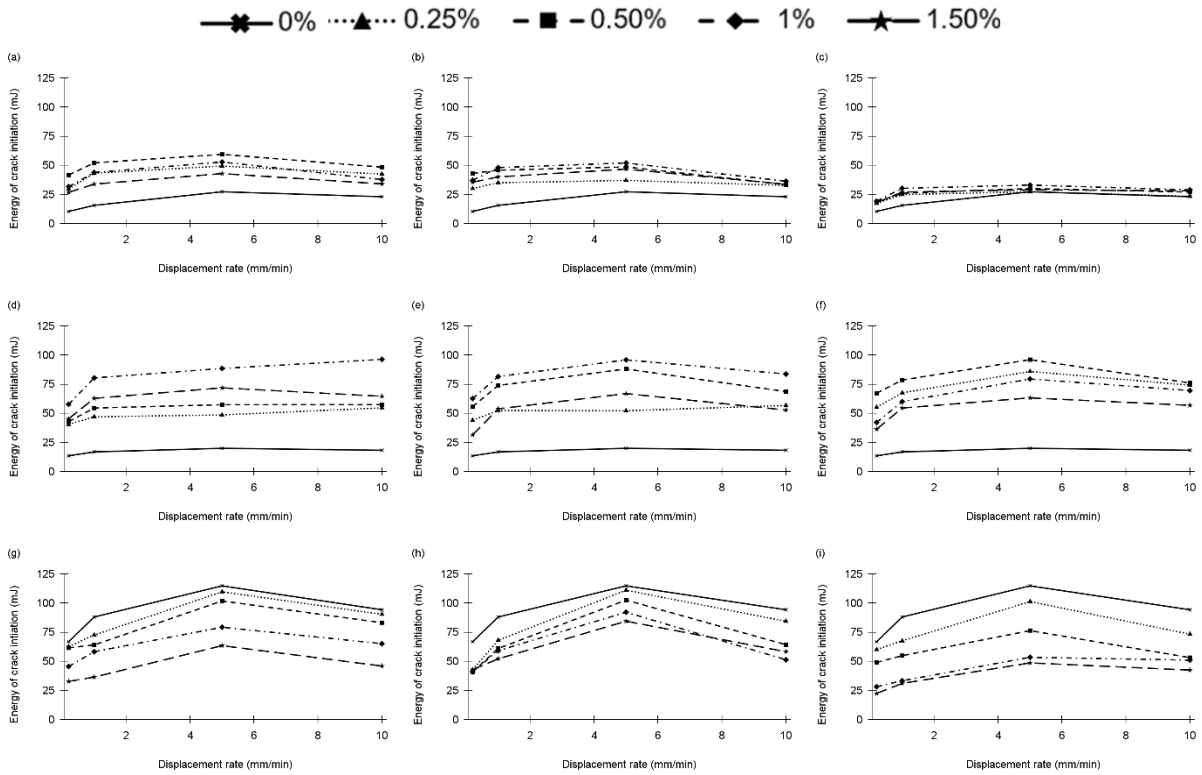

Figure 4.19. Effect of PP fiber in mode-II crack initiation energy under various displacement rates: (a) 6mm at 7 days, (b) 13mm at 7 days, (c) 19mm at 7 days, (d) 6mm at 28 days, (e) 13mm at 28 days, (f) 19mm at 28 days, (g) 6mm at 90 days, (h) 13mm at 90 days, and (i) 19mm at 90 days.

Figure 4.16 illustrates the mode-II crack initiation energy of FR-CPB under various displacement rates. The matrix dominates the formation of crack initiation energy, similar to that measured under mode-I loading conditions. For FR-CPB samples, there is a high shift of crack energy at low displacement rates. For instance, FR-CPB with a fiber content of 1% shows an increase of 28% as the displacement rate increases from 0.2mm/min to 1mm/min (Figure 4.19.d). The highest sensitivity was observed at 28 days, when the energy had a monotonic increase with the displacement rate. The critical displacement

rate changed from 1mm/min at 7 days to 5mm/min at advanced ages. Moreover, the sensitivity of FR-CPB samples at a higher displacement rate is reduced. This indicates the high crack deformation of the sample.

At 7 days, the sensitivity of the energy of crack initiation to displacement rate is higher when shorter fiber lengths are adopted. At 28 days, FR-CPB showed higher values than control CPB, and 1% fiber content was the critical fiber content. At 19mm, the critical fiber content reduced to 0.5%, indicating the fiber length effect is limited. Also, the increase in fiber length maintained a limited crack initiation energy range of 40 mJ to 90 mJ. At 90 days, the control CPB demonstrates a higher crack initiation energy than the FR-CPB samples (Figure 4.19 (g-i)). FR-CPB with low fiber content has higher energy across all fiber lengths. Like mode-I crack initiation energy, the shorter fiber length results in a stronger sensitivity to displacement rates.

4.5.3 Mode-III crack initiation energy under various displacement rates

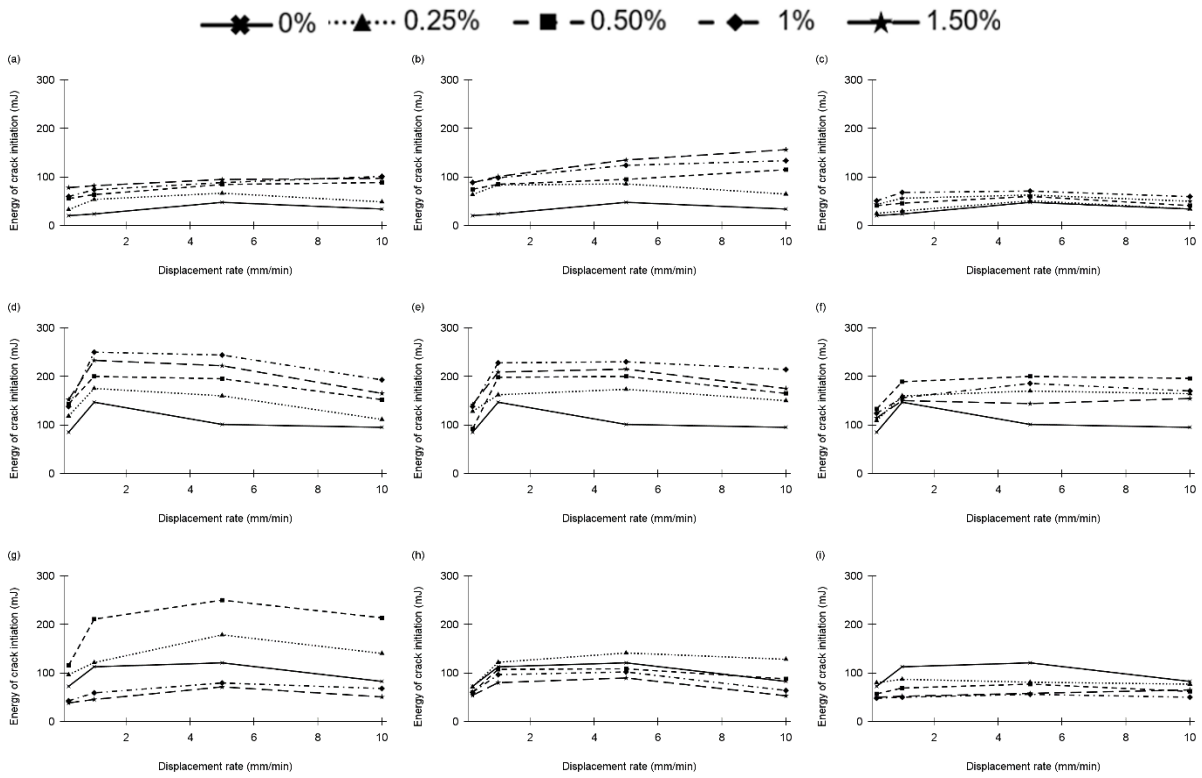

Figure 4.20. Effect of PP fiber in mode-III crack initiation energy under various displacement rates: (a) 6mm at 7 days, (b) 13mm at 7 days, (c) 19mm at 7 days, (d) 6mm at 28 days, (e) 13mm at 28 days, (f) 19mm at 28 days, (g) 6mm at 90 days, (h) 13mm at 90 days, and (i) 19mm at 90 days.

Figure 4.20 shows the changes in mode-III crack initiation energy of FR-CPB under different displacement rates. At 7 days, crack initiation energy shows limited sensitivity to displacement rates. The corresponding rate of change of crack initiation energy of FR-CPB and CPB illustrates no obvious variation with the displacement rates. At advanced ages, the sensitivity of crack initiation energy to displacement rates gradually improved, which can be attributed to the hardened matrix. At 28 days, crack initiation energy peaks under a displacement rate of 1mm/min. The degree of sensitivity gradually changed with displacement rates, indicating tension resistance exerted by the fiber. However, CPB is

more sensitive to changes in displacement rates from 0.2mm/min to 1mm/min with a rise of 42%, whereas FR-CPB demonstrates a 30% change in crack initiation energy (Figure 4.20.d). Contrasting to the mode-II loading condition, mode-III crack initiation energy is higher due to ENDB's high sample thickness, and more fracture energy is needed to promote crack growth.

Regarding fiber content, there was a monotonic increase in the mode-III crack initiation energy at early ages. At 28 days, 1% and 0.5% fiber content produce the highest crack initiation energy of FR-CPB with 6mm and 19mm fibers. For the FR-CPB with shorter fibers (i.e., 6mm), the resultant crack initiation energy intends to possess a monotonic increase with displacement rate. This can be attributed to the limited matrix space occupied by shorter fibers. The fiber inclusions negatively affect the integrity of the CPB matrix due to the weak interfacial transition zone between fibers and tailing particles, which weakens the frictional resistance of materials to the shear stress and thus influences the crack initiation energy. Finally, the fiber reinforcement effect gradually disappears with the progression of cement hydration. Alternatively, the crack initiation energy of control CPB without fibers shows the highest value compared with FR-CPB.

4.6 Effect of displacement rates on fracture energy

4.6.1 Mode-I fracture energy under various displacement rates

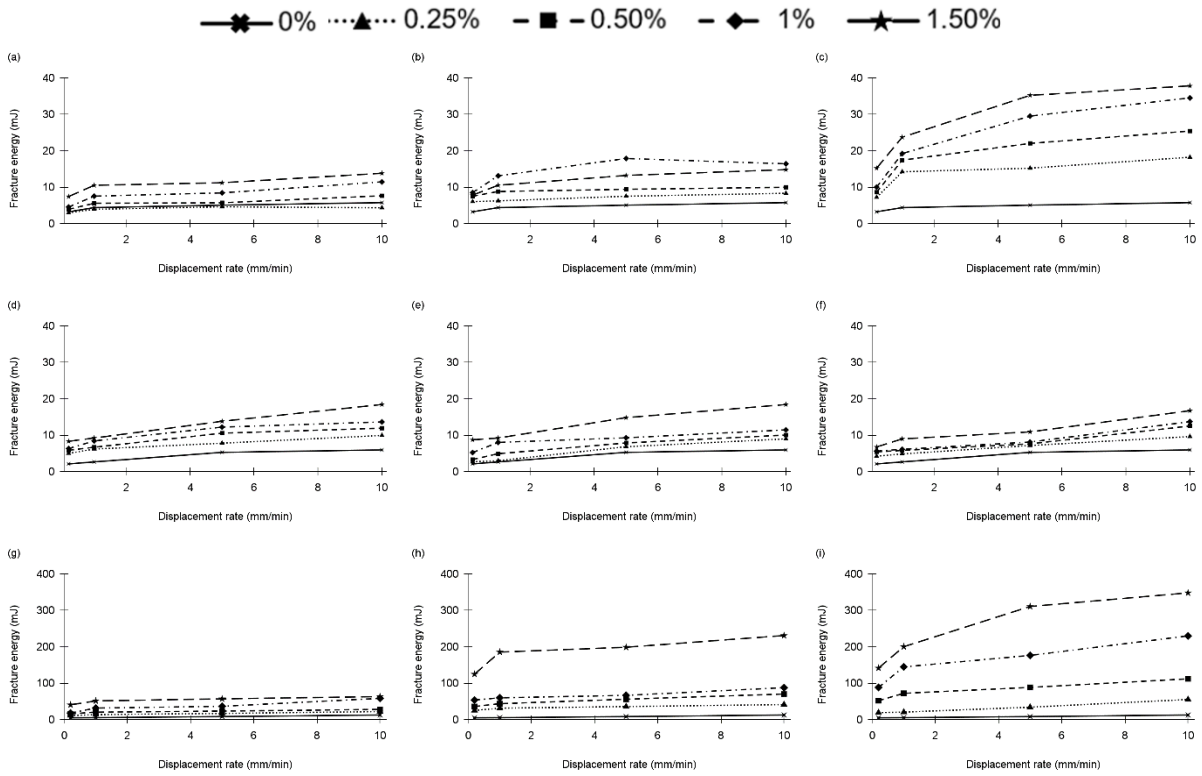

Figure 4.21. Effect of PP fiber in mode-I fracture energy under various displacement rates: (a) 6mm at 7 days, (b) 13mm at 7 days, (c) 19mm at 7 days, (d) 6mm at 28 days, (e) 13mm at 28 days, (f) 19mm at 28 days, (g) 6mm at 90 days, (h) 13mm at 90 days, and (i) 19mm at 90 days.

The influence of displacement rates on the fracture energy of FR-CPB is presented in Figure 4.21. It can be observed that the fracture energy of FR-CPB and CPB showed sensitivity to changes in displacement rates throughout the curing times. The sensitivity of fracture energy to displacement rates appears at 7 days. Meanwhile, 7 and 28 days of fracture energy is comparable to each other. It is observed that fracture energy possesses a monotonic increase with an increasing displacement rate. Through all curing time, the

displacement rate of 1mm/min can cause significant variation in the rate of change of fracture energy and thus can be considered a critical displacement rate, beyond which the rise of fracture energy is limited. The magnitude of fracture energy is observed to improve by ten times from 7 days to 90 days. This is due to the bonding interaction between the matrix and fiber at 90 days. As shown in Figure 4.21 (i), the sensitivity of fracture energy to displacement rate is more significant than that of other samples. This indicates that longer fibers can lead to a stronger dependence of fracture energy on displacement rates at advanced ages.

As fiber content and fiber length increase, fiber inclusion significantly contributes to the development of fracture energy under various loading rates. The increase in fiber content showed an increase in the value of fracture energy throughout all curing time. However, the rise in fiber length was the dominant factor at all curing times. For instance, at 90 days, the fiber length change from 6mm to 19mm showed an increase of 73% in fracture energy. Similar to the stiffness and fracture toughness, the evolutionary trend of fracture energy is consistent with control CPB with low fiber content and short fibers. However, as shown in Figure 4.21 (c) (f) and (i), FR-CPB with 19mm fibers shows significant changes in fracture energy when the fiber content is more important than 0.5%. Therefore, the observable improvement of fracture energy can confirm the effectiveness of fiber reinforcement on post-peak fracture resistance. Thus, fiber length dominates fracture energy values from the enclosed area from the post-peak trend.

4.6.2 Mode-II fracture energy under various displacement rates

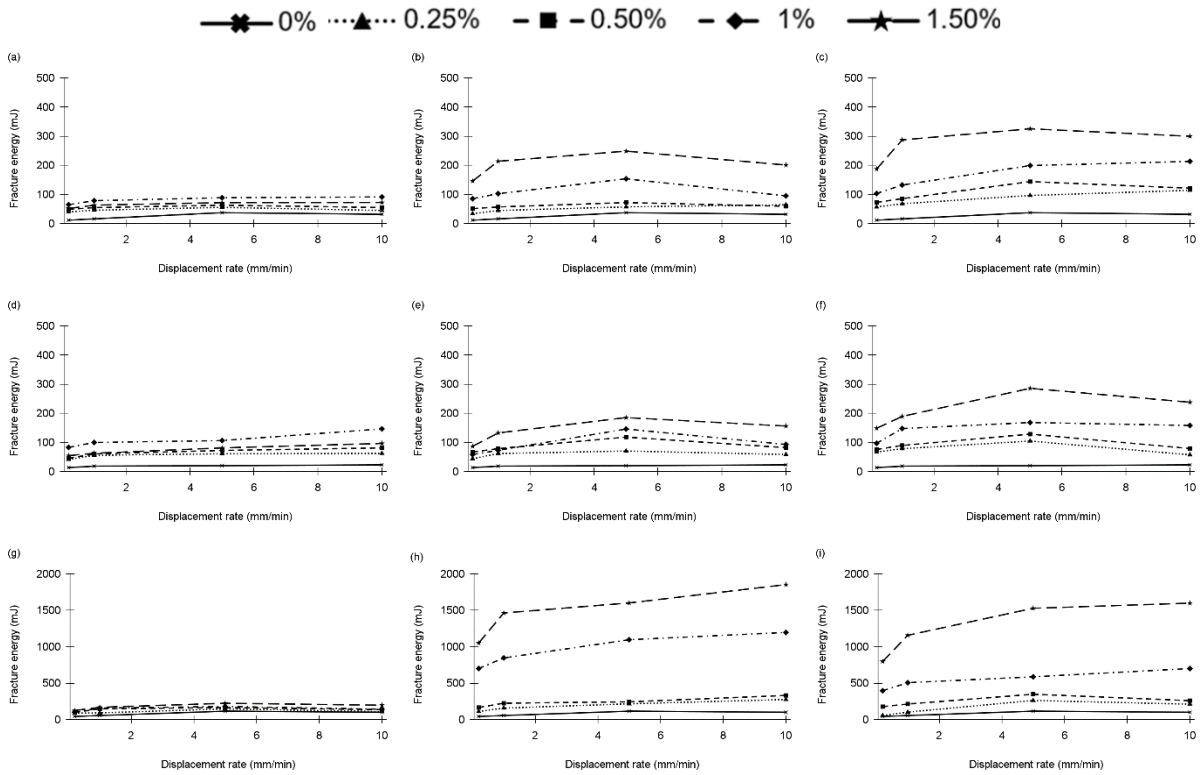

Figure 4.22. Effect of PP fiber in mode-II fracture energy under various displacement rates: (a) 6mm at 7 days, (b) 13mm at 7 days, (c) 19mm at 7 days, (d) 6mm at 28 days, (e) 13mm at 28 days, (f) 19mm at 28 days, (g) 6mm at 90 days, (h) 13mm at 90 days, and (i) 19mm at 90 days.

Figure 4.22 shows the evolution of mode-II fracture energy of FR-CPB under different displacement rates. Contrasting to mode-I fracture energy, mode-II fracture energy has a monotonic increase as the displacement rates increase up to 5mm/min, and then a reduced fracture energy appears under a further increase in displacement rates (i.e., 10mm/min). Similar to the influence of displacement rate on mode-I fracture energy, a critical displacement rate (1mm/min) can be identified for the mode-II fracture energy, resulting in considerable changes in the fracture energy. Moreover, the 7 and 28 days FR-CPB shows relatively weak dependence of fracture energy on the displacement rates,

except for 19mm, which showed enhanced sensitivity toward change in displacement rate (Figure 4.22 (c) and (f)). Similar to mode-I fracture energy, the sensitivity of fracture energy values toward displacement rate increases dramatically at 90 days.

At early ages, the rate of change in fracture energy is proportional to the adjustment in fiber content. The values of FR-CPB fracture energy are comparable at 7 and 28 days. This is because the weak reinforcement effect at early ages limits the enhancement of fracture energy. The 1.5% fiber content is observed to produce a higher fracture energy across all fiber lengths. The amount of fibers present in the matrix affects crack propagation. As discussed above, the fiber enhancement in mode-II post-peak resistance is well observed at the high fiber content. At 90 days, 13mm and 19mm fibers showed a higher improvement in fracture energy (Figure 4.22 (h)-(i)). However, the 13mm fibers produced more consistent results due to the preferable bonding interaction with the matrix. For instance, there is an 86% increase in the 90-day fracture energy from 6mm to 13mm and a 24% reduction as a further increase in fiber length from 13mm to 19mm for FR-CPB with 1.5% fiber content. Similar to mode-I fracture energy, fiber length imposes a more significant influence on the development of fracture energy over fiber content under mode-II loading conditions.

4.6.3 Mode-III fracture energy under various displacement rates

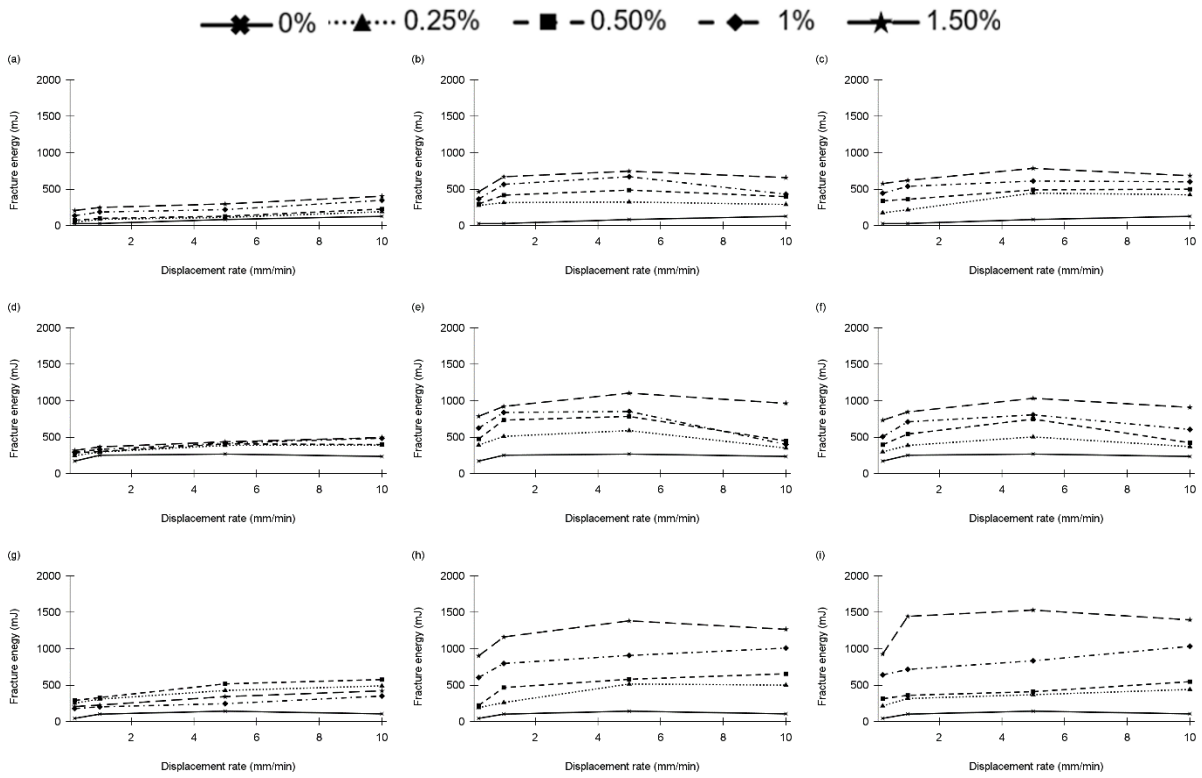

Figure 4.23. Effect of PP fiber in mode-III fracture energy under various displacement rates: (a) 6mm at 7 days, (b) 13mm at 7 days, (c) 19mm at 7 days, (d) 6mm at 28 days, (e) 13mm at 28 days, (f) 19mm at 28 days, (g) 6mm at 90 days, (h) 13mm at 90 days, and (i) 19mm at 90 days.

From Figure 4.23, it can be observed that the 7 days mode-III fracture energy is sensitive to the displacement rate and shows a linearly proportional increase with the displacement rate. At 28 days, a critical displacement rate of 5mm/min yields significant changes in mode-III fracture energy, beyond which a reduction in fracture energy is detected (Figure 4.23 (e)-(f)). As shown in Figure 4.23 (g), the sensitivity of fracture energy of FR-CPB with 19mm fibers is limited at 7 days, and a relatively weak monotonic increase can be observed as the displacement rate increases. At advanced ages, there is an obvious increase in mode-III fracture energy as the displacement rate increases to 1mm/min.

Similar to mode-I and mode-II fracture energy, 1.5% fiber content can produce the highest mode-II fracture energy for all fiber lengths. This indicates the critical role fiber content plays in the development of fracture energy. Under mode-III loading conditions, shorter fibers can weaken the sensitivity of fracture energy to displacement rate and thus yield relatively low fracture energy. For instance, there is a 23% increase in fracture energy of FR-CPB with a fiber content of 1.5% when the displacement rate changes from 0.2mm/min to 1mm/min and an 8% reduction in fracture energy when the displacement rate further increases from 1mm/min to 10mm/min (see Figure 4.23 (h)). Moreover, as fiber length continuously increases, the enhancement of mode-III fracture energy is observed across curing times. The longer fiber promotes the formation of a bridging effect in the cracked matrix and thus effectively enhances the fracture energy consumed by the FR-CPB under out-of-plane shear stress. Therefore, fiber length plays a crucial role in the development of fracture energy of FR-CPB under various loading conditions.

Chapter Five Conclusions and Recommendation

5.1 Conclusions

This thesis studies the fracture behavior and properties of FR-CPB under different displacement rates (0.2mm/min, 1mm/min, 5mm/min, and 10mm/min) from early to advanced ages (7 days, 28 days, and 90 days). Moreover, to offer an in-depth insight into the loading-rate-dependent behavior of FR-CPB, the effect of fiber length (6mm, 13mm, and 19mm) and fiber content (0%, 0.25%, 0.5%, 1%, and 1.5%) were examined. Based on the obtained results, the main conclusions are summarized as follows:

1. The displacement rate imposes a more significant influence on the fracture behavior and properties at advanced ages. Both pre and post-peak response of FR-CPB demonstrates changes under different displacements. Specifically, FR-CPB showed a linear response in the pre-peak slope under various displacement rates, which confirms the effectiveness of linear elastic fracture mechanics to the pre-peak behavior of FR-CPB materials. Moreover, higher displacement rates cause higher peak load and post-peak resistance under mode-I loading conditions. The stronger sensitivity of fracture behavior to the displacement rate confirms the dominant role played by the CPB matrix at advanced ages.

2. Under the mode-II loading condition, the 5mm/min displacement rate results in a higher peak load, making it a critical displacement rate. The CPB matrix dominates the pre-peak, showing a higher sensitivity to various displacement rates. For the post-peak response, FR-CPB shows a sudden drop after the peak load and is immediately

followed by post-peak resistance, which can be attributed to the bridging effect of fibers under in-plane shear stress. Moreover, the post-peak response is governed by fiber reinforcement, which has a relatively weak sensitivity to changes in displacement rates. At higher fiber content (1% and 1.5%), the enhancement of post-peak resistance becomes more obvious under mode-II loading conditions.

3. Under the mode-III loading condition, the 1mm/min displacement rate leads to a higher peak load, making it a critical displacement rate. The pre-peak slopes are similar to each other at various displacement rates. At the post-peak stage of FR-CPB, a secondary post-peak resistance, i.e., pseudo-hardening behavior, is widely observed under mode-III loading condition, which indicates the unique mechanisms responsible for the mode-III post-peak behavior of FR-CPB. The pseudo-hardening behavior is closely related to the edge-cutting effect of fibers under out-of-plane shear stress.

4. FR-CPB and control CPB consistently demonstrate a considerable improvement in fracture toughness from early to advanced ages. The fiber inclusion increased peak load due to the bonding interaction between fiber and matrix.

5. The CPB and FR-CPB stiffness and energy of crack initiation have similar trend under various displacement rates. The dominant factor for the loading-rate-dependent fracture properties can be attributed to the CPB matrix. Consequently, a stronger sensitivity of fracture properties to the displacement rates has been repeatedly observed at 90 days. Higher fiber content adversely affects the development of 90-

day stiffness under various displacement rates. However, short fiber can lead to a greater extent of discrepancy of stiffness at 90 days.

6. A critical displacement rate of 1mm/min exists and significantly affects the rate of change in fracture properties of FR-CPB under various loading conditions. A sharp increase in fracture properties has been measured as the displacement rate increases from 0.2mm/min to 1mm/min. Although a continuous improvement was measured, the rate of change in stiffness, fracture toughness, and crack initiation energy became smaller. This can be attributed to the changes in pore water pressure and matrix structure. Under a low displacement rate, the CPB matrix has adequate time to dissipate the excess pore water pressure, thus developing a stronger particle resistance.

7. Fracture toughness, stiffness, and crack initiation energy values mainly depend on fiber content other than fiber length. In contrast, fracture energy depends more on fiber length, especially when fiber length reaches 13mm. The critical fiber content of 0.5% can be considered an optimum fiber content for the usage of synthetic fiber in CPB technology.

5.2 Recommendation for future work

The main recommendation of this work is to continue the research of CPB technology to the point of engineering design. Those works can enhance the understanding of tailing management efficiently and effectively. More studies can be performed by increasing the displacement rate to 1000mm/min and observing how FR-CPB would behave in dynamic

loading rates. The increase in displacement rate would clarify the critical displacement rate value for mode-I testing and the fractural behavior of samples, especially at post-peak. Also, FR-CPB can be experimented with other fibers that could optimize post-peak behavior, reduce cost, and improve stiffness. Undergoing more experiments by increasing fiber content in mode-III can specify the post-peak resistance and the effectiveness of fiber.

To make FR-CPB cost-effective, financial-based research is needed to calculate the money required to manage tailings with the existence of fiber is advisable. Lastly, those improvements can gradually develop the understanding of fracture behaviors in underground mining and tailing management using FR-CPB. Meanwhile, the development of predictive models should be prioritized to understand better and forecast the behavior of fiber-reinforced backfills under various conditions. These models can help optimize mixture designs and predict performance outcomes more accurately, thereby aiding in the efficient use of resources. Sensitivity percentage analysis on the effect of fiber content and fiber length in FR-CPB against various displacement rates. Regression and variance analysis can be implemented as pre-peak is primarily linear, and post-peak is non-linear. Also, a new form of experimental design can be practiced to reduce the time and total sample number used for future research.

Moreover, future studies should explore the microstructural interactions between fibers and cementitious matrices better to understand the mechanisms behind strength enhancement and crack resistance. Additionally, acoustic emission (AE) monitoring can provide valuable insights into the damage precursors and energy dissipation

characteristics of fiber-reinforced backfills, further elucidating the role of fibers in improving material performance. By focusing on these areas, future research can significantly advance the field of fiber-reinforced mine backfill materials, leading to safer and more sustainable mining operations.

Reference

1. A. Ghirian, M. Fall. Properties of cemented paste backfill. *Paste Tailing Manag, 2017.*
2. A. MRM, Bahmani A, Akhondi S. Determination of mode III fracture toughness for different materials using a new designed test configuration. Mater Des. 2015;86: 863–871.
3. Al-Mashhadani, O. Canpolat, Y. Aygormez, M. Uysal, S. Erdem, Mechanical and microstructural characterization of fiber-reinforced fly ash based geopolymer composites, *Constr. Build. Mater. 167 (2018) 505–513.*
4. B. Tikou, B. Bussiere, and M. Benzaazoua. Mechanical behavior of cemented paste backfills. *Research gate, Jan 2000, 53rd Annual conf. of the Canadian Geotechnical Society, Vol. 1, ISBN 0-920505-15-5.*
5. Belem, T. Benzaazoua, M. Bussière, B. Dagenais, 2002. Effects of settlement and drainage on strength development within mine paste backfill. In: *Proceedings of the 9th Inter. Conf. on Tailings and Mine Waste, 27–30 January, pp. 139–148.*
6. C. Yu, M. Zhu, X. Shong, Y. Chen, Study on dyeable polypropylene fiber and its properties, *J. Appl. Polym. Sci. 82 (13) (2001) 3172–3176.*
7. C.S. Tang, B. Shi, W. Gao, F.J. Chen, Y. Cai, Strength and mechanical behavior of short polypropylene fiber reinforced and cement stabilized clayey soil, *Geotext. Geomembrane, 25 (3) (2007) 194–202.*

8. C.S. Tang, B.Shi, W. Gao, F.J. Chen, Y. Cai, Strength and mechanical behavior of short polypropylene fiber reinforced and cement stabilized clayey soil, *Geotext, Geomembr. 25(3) 2007 194-202.*
9. Cao S, Yilmaz E, Song WD. Assessment of viscosity, strength, and microstructural properties of cemented tailings backfill. *Miner. 2018; 8: 352.*
10. Cao, S., Yilmaz, E., & Song, W. Fiber type effect on strength, toughness and microstructure of early age cemented tailings backfill. *Cons. and Buil. Mater., 2019.*
11. C. Qi, A. Fourie. Cemented paste backfill for mineral management: Review and future perspectives. *Miner. Eng., 144, 2019.*
12. C. NC, N. HP, Silva AP, Sosnoski J. Durability and strength of fiber-reinforced compacted gold tailings cement blends. *Geotext Geome. 2017; 45: 98–102.*
13. Consoli NC, Thome A, Girardello V, Ruver CA. Uplift behavior of plates embedded in fiber-reinforced cement stabilized backfill. *Geotext Geome. 2012;35: 107–11.*
14. Deb, D., Sreenivas, T., Dey, G.K., Panchal, S., 2017. Paste backfill technology: Essential characteristics and assessment of its application for mill rejects of uranium ores. *Trans. Indian Inst. Met. 70, 487–495.*
15. Deng ZC, Feng Q. Fracture properties of hybrid fibers reinforced reactive powder concrete. *J Build Mater 2016;19(1):14–21.*
16. E. Yilmaz, M. Benzaazoua, T. Belem, B. Bussière, Effect of curing under pressure on compressive strength development of cemented paste backfill, *Miner. Eng. 22 (9-10) (2009) 772–785.*

17. E.B. Pereira, G. Fischer, J.A.O. Barros, M. Lepech. Crack formation and tensile stress-crack opening behavior of fiber reinforced cementitious composites (FRCC). *Korea Concrete Inst., 2010.*

18. Edraki, M., Baumgartl, T., Manlapig, E., Bradshaw, D., Franks, D.M., Moran, C.J. Designing mine tailings for better environmental, social and economic outcomes: a review of alternative approaches. *J. Cleaner Prod. 84, 411–420, 2014.*

19. E. Araujo, D. Simon, F. Franxa, O. Neto and O. Junior. Shear strength of a cemented paste backfill submitted to high confining pressure. *App. Mech. and Mater., 2017 vol 858, pp 219-224.*

20. Fahey, M., Helinski, M., and Fourie, A. 2009. Some aspects of the mechanics of arching in backfilled stopes. *Can. Geotech. J., 4611, 1322–1336.*

21. Fang, K. and Fall, M. 2018. Effects of curing temperature on shear behavior of cemented paste backfill-rock interface, *Inter. J. of Rock Mech. and Mining Sci., 112: 184- 192.*

22. Farina I, Modano M, Zuccaro G, Goodall R, Colangelo F. Improving flexural strength and toughness of geopolymer mortars through additively manufactured metallic rebars. *Compos B Eng 2018; 145: 155–61.*

23. F. Gong, H. Ye, and Y. Luo. The effect of high loading rate on the behavior and mechanical properties of coal-rock combined body. *H., shock and vibration volume 2018, Art. ID 4374530, 9 pages.*

24. G.L, Xue, E, Yilmaz, W.D, Song, Influence of fiber reinforcement on mechanical behavior and microstructural properties of cemented tailings backfill, *Constr. Build Mater. 213 (2019) 275-285.*
25. G. Xue, E. Yilmaz, G. Feng, S. Cao, L. Sun. Reinforcement effect of polypropylene fiber on dynamic properties of cemented tailings backfill under SHPB impact loading. *Constr. Build Mater., volume 279, 2021*.
26. G. Xue, E. Yilmazz, W. Song, S. Cao. Mechanical, flexural and microstructural properties of cement-tailings matrix composites: Effects of fiber type and dosage. *Com. Part B, 2019, 131-142.*
27. H. Soleimani Fard, D. Konig, M. Goudarzy, Plane strain shear strength of unsaturated fiber reinforced fine-grained soils, *Acta Geotech. (2021) 1-9.*
28. H. Qin, S. Cao, and E. Yilmaz. Mechanical, energy evolution, damage and microstructural behavior of cemented tailings-rock fill considering rock content and size effects. *Con. Build Mater. 411 (2024) 134449.*
29. Hassani, F., and Archibald, J. 1998. *Mine backfill, CD-ROM 263p.*
30. I. Libos, Liang Cui, Xinrong Liu. Effect of Curing temperature on time-dependent shear behavior and properties of polypropylene fiber reinforced cemented paste backfill, *Constr. Build Mater. 311 (2021).*
31. I. Libos, Liang Cui. Mechanical properties and behavior of early-age fiber-reinforced cemented paste backfill. *Inter. Conf. on civil structural and transportation eng., 2020, 193.*

32. J. Lu, D. Zhang, G. Huang, X. Li, H. Gao, G. Yin, Effects of loading rate on the compound dynamic disaster in a deep underground coal mine under true triaxial stress, *Int. J. Rock. Mech. Min. 134 (2020) 104453.*

33. J.J. Li, J.G. Niu, C.J. Wan, B. Jin, Y.L. Yin, Investigation on mechanical properties and microstructure of high-performance polypropylene fiber reinforced lightweight aggregate concrete, *Constr. Build Mater. 118 (2016) 27–35.*

34. Jiaxu Jin, Chengju Li, Shihao Yuan, Qi Sun, and Hui Yang. Effect of fiber on early strength and interface stiffness of cemented tailings backfill. *Mater. Res. Express 9, (2022) 045202.*

35. Kim SH, Heo Y-J, Park m, Min B-G, Rhee KY, Parl S-J. Effect of hydrophilic graphite flake on thermal conductivity and fracture toughness of basalt fibers/epoxy composites. *Compos B Eng 2018; 153: 9–16.*

36. Koohestani B.; Koubaa, A.; Belem, T.; Bussière, B.; Bouzahzah. H. Experimental investigation of mechanical and microstructural properties of cemented paste backfill containing maple-wood filler. *Constr. Build. Mater. 2016, 121, 222–228.*

37. K. Fang, and Liang Cui. Experimental investigation of fiber content and length on curing time-dependent mode-I fracture behavior and properties of cemented paste backfill and implication to engineering design. Fatigue and Fracture of Eng. materials and structures, 2022.

38. K. Fang, J. Zhang, Liang Cui, Sada Huruna, and Meng Li. Cost optimization of cemented paste backfill: State of the art review and future perspectives. *Mine. Eng. 204 (2023) 108414.*

39. K. Fang, M. Fall. Chemically induced changes in the shear behavior of interface between rock and tailings backfill undergoing cementation*, Rock Mech. and Rock Eng., volume 52, page 3047-3062, 2019.*
40. K. Fang, M. Fall. Shear Behavior of Rock-Tailings Backfill Interface: Effect of cementation, rock type, and rock surface roughness. *Geote. and Geo. Eng., volume 39, pages 1753-1770, 2021.*
41. K. Fang, M. Fall. Shear Behavior of the interface between rock and cemented backfill: Effect of curing stress, drainage condition and backfilling rate. *Rock Mech. and Rock Eng., volume 53, pages 325-336, 2020.*
42. L. Cui and M. Fall. Modeling of self-desiccation in a cemented backfill structure. *Int. J. for Num. and Anal. Methods in Geo., vol. 42, no.6.*
43. L. Wang, B. Ji, Y. Hu, R. Liu, W. Sun, A review on in situ phytoremediation of mine tailings, *Chemo. 184 (2017) 594–600.*
44. Li J, Cao S, Yilmaz E, Liu Y. Compressive fatigue behavior and failure evolution of additive fiber-reinforced cemented tailings composites. *Int. J. Miner Metall Mater. 2022; 29: 345–355.*
45. L. Cui, A. McAdie. Experimental study on evolutive fracture behavior and properties of sulfate-rich fiber-reinforced cemented paste backfill under pure mode-I, mode-II and mode-III loading. *Int. J. of rock Mech. and Mining Sci. 169 (2023) 105434.*

46. L. Cui, S. Singalreddy, Guanlong Guo. Geomechanical behavior and properties of cemented paste backfill under passive interface loading and their influences on field-scale stability. *Acta Geotechnical, volume 18, pages 3927-3945, 2023.*

47. M. D. Kuruppu, Y. Obara, M. R. Ayatollahi, K. P. Chong, T. Funatsu. ISRM suggested method for determining the mode I static fracture toughness using a semi-circular bend specimen: *Curtin University, Dep. of Geological Eng., 2017.*

48. M. Fall, D. Adrien, J.C. Célestin, M. Pokharel, M. Touré, Saturated hydraulic conductivity of cemented paste backfill, *Miner. Eng. 22 (15) (2009) 1307– 1317.*

49. M.R. Ayatollahi, M.R.M. Aliha. On determination of mode II fracture toughness using semi-circular bend specimen. *Inte. J. of solids and structures 43, 2006, 5217-5227.*

50. M. GW, L. ZJ, Y. XW, G. LJ. Macro-meso experiment of fiber-reinforced cement paste filling material. *J Beijing Univ Technol 2016; 42(3): 406–412.*

51. Marcos G., A. Enfedaque, M. V. Faria, M. Ruiz. The potential of fiber-reinforced concrete to reduce the environmental impact of concrete *construction. App. Sci., 2024, 14 (15), 6629.*

52. Matthew Helinski, Martin Fahey, and Andy Fourie. Behavior of cemented paste backfill in two mine stopes: measurements and modeling. *J. of Geotech. and Geoenv. Eng., July 2010.*

53. Mingchao Liu, Yixiang Gan, Dorian A.H. Hanaor, Bin Liu, Changqing Chen. An improved semi-analytical solution for stress at round-tip notches. *Engineering Fracture Mechanics, 149 (2015), 134-143.*
54. N. Ranjbar, S. Talebian, M. Mehrali, C. Kuenzel, H.S.C. Metselaar, M.Z. Jumaat, Mechanisms of interfacial bond in steel and polypropylene fiber reinforced geopolymer composites, *Compos. Sci. Technol. 122 (2016) 73–81*.
55. N.C. Consoli, J.P. Montardo, M. Donato, D.M. Prietto, Effect of material properties on the behavior of sand-cement-fiber composites, Ground Improv. 8 (2) (2004) 77–90.
56. Nezhad MG, Tabarsa A, Latifi N. Effect of natural and synthetic fibers reinforcement on California bearing ratio and tensile strength of clay. *J Rock Mech Geotech Eng. 2021;13(3):626–642.*
57. Okubo, S., Nishimatsu, Y., and He, C. (1990). Loading Rate Dependence of Class II Rock Behavior in Uniaxial and Triaxial Compression Tests Application of a Proposed New Control Method. *Int. J. Rock Mech. Mining Sci. Geomechanics Abstr. 27 (6), 559–562.*
58. P. Sukontasukkul, P. Pongsopha, P. Chindaprasirt, S. Songpiriyakij, Flexural performance and toughness of hybrid steel and polypropylene fiber-reinforced geopolymer, *Constr. Build. Mater. 161 (2018) 37–44.*
59. Pakravan HR, Latifi M, Jamshidi M. Hybrid short fiber reinforcement system in concrete: a review. *Constr Build Mater 2017; 142: 280–94.*

60. Peter C. Hewlett and Martin Liska. Lea's chemistry of cement and concrete. Fifth edition, 2019.
61. S. Akbulut, S. Arasan, E. Kalkan, Modification of clayey soils using scrap tire rubber and synthetic fibers, *Appl. Clay Sci. 38 (1–2) (2007) 23–32*.
62. S. Cao, G. Xue, E. Yilmaz, Z. Yin, Assessment of rheological and sedimentation characteristics of fresh cemented tailings backfill slurry, *Int. J. Min., Reclam. Environ. 35 (5) (2021) 319–335.*
63. Sami Hasan and Liang Cui. Evolutive fracture behavior of cemented paste backfill. Lakehead University Library, 2022.
64. Sheng Huang, Kaiwen Xia, and Lan Qiao. Dynamic tests of cemented paste backfill: effects of strain rate, curing time and cement content on compressive strength. *Journal Material Science (2011) 46: 5165-5170.*
65. Shuai Cao, Erol Yilmaz and Weidong Song. Fiber type effect on strength, toughness and microstructure of early-age cemented tailings backfill. *Construction and Building Materials 223, 2019, 44-54.*
66. Sun Q, Zhang J, Zhou N. Study and discussion of short-strip coal pillar recovery with cemented paste backfill. *Int J Rock Mech Min. 2018; 104:147–155.*
67. T. Belem, M. Benzaazoua, B. Bussière, Mechanical behavior of cemented paste backfill, *53rd Annual Conf. of the Canadian Geotechnical Society, Montreal, Canada. (2000).*
68. T. Belem, M. Benzaazoua, Design and application of underground mine paste backfill technology, *Geotech. Geol. Eng. 26 (2) (2008) 147–174.*

69. T. Yetimoglu, O. Salbas, A study on shear strength of sands reinforced with randomly distributed discrete fibers*, Geotext. Geomembr. 21 (2)* 2003, 103-110.
70. Veronique Lazarus, F.-G. Buchholz, M. Fulland, J. Wiebesiek. Comparison of predictions by mode II or mode III criteria on crack front twisting in three or four-point bending experiments. *International Journal of Fracture, 2008, 153 (2), pp.141-151.*
71. W. Abbass, M.I. Khan, S. Mourad, Evaluation of mechanical properties of steel fiber-reinforced concrete with different strengths of concrete, *Constr. Build. Mater. 168 (2018) 556–569.*
72. W.A. Hustrulid, W.A. Hustrulid, R.C. Bullock, R.L. Bullock, Underground mining methods: *Engineering fundamentals and international case studies, SME2001.*
73. Wang Kun, Fu Jian-Xin, Wang Yu. PFC2D-Based Analysis of the Effect of the Axial Loading Rate on the Mechanical Properties of Backfill. *Advances in Materials Science and Engineering, 2023.*
74. Wang R, Zeng F, Li L. Stability analyses of side-exposed backfill considering mine depth and extraction of adjacent stope. *Int J Rock Mech Min. 2021;142, 104735.*
75. Wasantha, P. L. P., Ranjith, P. G., Zhao, J., Shao, S. S., and Permata, G. (2015). Strain Rate Effect on the Mechanical Behaviour of Sandstones with Different Grain Sizes. *Rock Mech. Rock Eng. 48 (5), 1883–1895.*
76. Wenbin Xu, Qianlong Li, and Yalun Zhang. Influence of temperature on compressive strength, microstructure properties, and failure pattern of fiber-

reinforced cemented tailings backfill. *Construction and Building Materials 222 (2019), 776-785.*

77. X.X. Zhang, G. Ruiz, R.C. Yu, M. Tarifa, Fracture behavior of high-strength concrete at a wide range of loading rates. *International Journal of Impact Engineering 36(10) (2009) 1204-1209.*

78. X.X. Zhang, R.C. Yu, G. Ruiz, M. Tarifa, M.A. Camara, Effect of loading rate on crack velocities in HSC. *International Journal of Impact Engineering 37(4) (2010) 359-370.*

79. Xiangqian Xu, Ni An, and Kun Fang. Experimental investigation into the temperature effect on the shear behavior of the fiber-reinforced interface between rock and cemented paste backfill. *Construction and Building Materials 356 (2022) 129280.*

80. Xin Chen, Xiuzhi Shi, Jian Zhoa, Enming Li, peiyong Qiu, Yonggang Gou. High strain rate compressive strength behavior of cemented paste backfill using split Hopkinson pressure bar. *International Journal of Mining Science and Technology, volume 31, 2021, 387-399.*

81. Xin Chen, Xiuzhi Shi, Shu Zhang, Hui Chen, Jian Zhou, and Peisheng Hunag. Fiber-reinforced cemented paste backfill: The effect of fiber on strength properties and estimation of strength using nonlinear models. *Multidisciplinary Digital Publishing Institute, 2020.*

82. Xu WB, Cao PW, Tian MM. Strength development and microstructure evolution of cemented tailings backfill containing different binder types and contents. *Minerals 2018; 8: 167.*
83. Xu X, Fall M, Alainachi I, Fang K. Characterisation of fiber-reinforced backfill/rock interface through direct shear tests. *Geotech Res. 2020;7(1):11–25.*
84. Xuepeng Song, Junbiao Li, Shi Wang, Shuang Zhou, Wu Liu, Yuankai Zhai, Yuxin Hao. Study of mechanical behavior and cracking mechanism of prefabricated fracture cemented paste backfill under different loading rates from the perspective of energy evolution. *Construction and Building Materials 361, 2022, ID 129737.*
85. Y. Li, L. Jin, L. Zhang. Long-term strengthening effect of cemented tailings considering the loading rates. *Electron. J. Geotech, 21, 2016, 955-968.*
86. Y. Wang, Q. Na, L. Zhang, Monitoring of in-situ properties for cemented tailings backfill that under drainage condition, *Constr. Build. Mater. 356 (2022), 129254.*
87. Yafei Hu, Keqing Li, Bo Zhang , Bin Han. Development of Cemented Paste Backfill with Superfine Tailings: Fludity, Mechanical Properties, and Microstructures Characteristics. *Materials 2023, 16(5), 1951.*
88. Yang Tang, Hailong Zhang, Jiang Xu, Seisuke Okubo and Xinrong Liu. Loading rate dependence of rock strength under triaxial compression. *Journals Frontiers in earth science Sep 2021, volume 9, Article ID 728366.*
89. Yang Tang, Seisuke Okubo Jiang Xu, Hailong Zhang, and Shoujian Peng. Loading-Rate Dependence of Rocks in Postfailure Region under Triaxial

Compression. *Journals Frontiers in earth science Sep 2018, volume 9, Article ID 1496127, 12 pages.*

90. Yi XW, Ma GW, Fourie A. Compressive behavior of fiber-reinforced cemented paste backfill. *Geotext Geomembranes 2015; 43: 207–15.*
91. Yilmaz E. Stope depth effect on field behavior and performance of cemented paste backfills. I*nt J Min Reclamat Environ. 2018;32(4):273–296.*
92. Z. Blikharskyy, R. Vashkevych, P. Vegera, Y. Blikharskyy. Crack Resistance of RC Beams on the Shear. *Proceedings of CEE, 2019.*
93. Z. Xiu, S. Wang, Y. Ji, F. Wang, F. Ren, Experimental study on the triaxial mechanical behaviors of the cemented paste backfill: Effect of curing time, drainage conditions and curing temperature, *J. Environ. Manag. 301 (2022), 113828.*
94. Zhang, B., Xin, J., Liu, L., Lijie, G., and Song, K. An Experimental Study on the Microstructures of Cemented Paste Backfill during Its Developing Process, *Advances in Civil Engineering, 2018.*
95. Zhanguo Xiu, Shuhong Wang, Yingchun Ji, Feili Wang, Fengyu Ren, Van-Tuan Nguyen. Loading rate effect on the uniaxial compressive strength (UCS) behavior of cemented paste backfill. *Construction and building materials, 2021, volume 271.*